

**This is an electronic reprint of the original article.
This reprint *may differ* from the original in pagination and typographic detail.**

Author(s): ALICE Collaboration

Title: Measurement of deuteron spectra and elliptic flow in Pb–Pb collisions at $\sqrt{s_{NN}} = 2.76$ TeV at the LHC

Year: 2017

Version:

Please cite the original version:

ALICE Collaboration. (2017). Measurement of deuteron spectra and elliptic flow in Pb–Pb collisions at $\sqrt{s_{NN}} = 2.76$ TeV at the LHC. *European Physical Journal C*, 77, Article 658. <https://doi.org/10.1140/epjc/s10052-017-5222-x>

All material supplied via JYX is protected by copyright and other intellectual property rights, and duplication or sale of all or part of any of the repository collections is not permitted, except that material may be duplicated by you for your research use or educational purposes in electronic or print form. You must obtain permission for any other use. Electronic or print copies may not be offered, whether for sale or otherwise to anyone who is not an authorised user.

Measurement of deuteron spectra and elliptic flow in Pb–Pb collisions at $\sqrt{s_{NN}} = 2.76$ TeV at the LHC

ALICE Collaboration*

CERN, 1211 Geneva 23, Switzerland

Received: 26 July 2017 / Accepted: 12 September 2017

© CERN for the benefit of the ALICE collaboration 2017. This article is an open access publication

Abstract The transverse momentum (p_T) spectra and elliptic flow coefficient (v_2) of deuterons and anti-deuterons at mid-rapidity ($|y| < 0.5$) are measured with the ALICE detector at the LHC in Pb–Pb collisions at $\sqrt{s_{NN}} = 2.76$ TeV. The measurement of the p_T spectra of (anti-)deuterons is done up to 8 GeV/c in 0–10% centrality class and up to 6 GeV/c in 10–20% and 20–40% centrality classes. The v_2 is measured in the $0.8 < p_T < 5$ GeV/c interval and in six different centrality intervals (0–5, 5–10, 10–20, 20–30, 30–40 and 40–50%) using the scalar product technique. Measured π^\pm , K^\pm and $p+\bar{p}$ transverse-momentum spectra and v_2 are used to predict the deuteron p_T spectra and v_2 within the Blast-Wave model. The predictions are able to reproduce the v_2 coefficient in the measured p_T range and the transverse-momentum spectra for $p_T > 1.8$ GeV/c within the experimental uncertainties. The measurement of the coalescence parameter B_2 is performed, showing a p_T dependence in contrast with the simplest coalescence model, which fails to reproduce also the measured v_2 coefficient. In addition, the coalescence parameter B_2 and the elliptic flow coefficient in the 20–40% centrality interval are compared with the AMPT model which is able, in its version without string melting, to reproduce the measured $v_2(p_T)$ and the $B_2(p_T)$ trend.

1 Introduction

The study of light (anti-)nuclei produced in relativistic heavy-ion collisions allows us to investigate the expansion and cooling down of the hot dense medium produced in heavy-ion collisions, the Quark Gluon Plasma (QGP), and the hadronisation mechanism. Proton and deuteron p_T spectra measured at the LHC by A Large Ion Collider Experiment (ALICE) [1], show a clear dependence on the charged particle multiplicity, which can be explained by models that take into account

the radial expansion of the emitting particle source [2]. To investigate different production scenarios, other observables, such as the coalescence parameter (B_A), which corresponds to the nucleons coalescence probability, and the elliptic flow (v_2) of light nuclei as a function of the transverse momentum, have been already studied at SPS, RHIC and LHC [2–5]. The B_A values at higher p_T complement the available results [2]. Measurements of the elliptic flow [6] allow for the investigation of collective effects among produced particles. The angular distribution of all the reconstructed charged particles with respect to the symmetry plane Ψ_n [7] can be expanded into a Fourier series

$$E \frac{d^3N}{dp^3} = \frac{1}{2\pi} \frac{d^2N}{p_T dp_T dy} \left(1 + \sum_{n=1}^{\infty} 2v_n \cos(n(\varphi - \Psi_n)) \right), \quad (1)$$

where E is the energy of the particle, \vec{p} the momentum, φ the azimuthal angle, y the rapidity, Ψ_n the angle of the spatial plane of symmetry of harmonic n [8–10] and

$$v_n = \langle \cos(n(\varphi - \Psi_n)) \rangle. \quad (2)$$

The second term of the Fourier series (v_2) is called elliptic flow. It is directly linked to the almond shaped overlap region of the colliding ions in non central interactions and it can be related to the hydrodynamic properties of the QGP [11]. It is thus sensitive to the system conditions in the early stages of the evolution of a heavy-ion collision [7]. For identified hadrons v_2 gives details about the hadronization mechanism. The deuteron is a pn bound state, whose binding energy (~ 2.24 MeV) is about two orders of magnitude lower than the hadronisation temperature. Thus if it is produced at hadronisation, it is likely that it would suffer from medium induced breakup in the hadronic phase. The v_2 measurements for d and \bar{d} provide an important test for the universal scaling of the elliptic flow [12] since it is expected to scale both with the v_2 of its constituent hadrons and with the v_2 of the constituent quarks.

This publication is dedicated to the memory of our colleague H. Oeschler who recently passed away.

* e-mail: alice-publications@cern.ch

Comparing the measured azimuthal anisotropy of the deuteron momentum distributions to the proton distributions, the STAR experiment [5] observed a mass number scaling in the $0.3 < p_T < 3$ GeV/ c region leading to the conclusion that the mechanism of light nuclei formation at RHIC energies is mainly due to the coalescence of hadrons.

In this paper (anti-)deuterons transverse-momentum spectra and elliptic flow v_2 measured by ALICE in Pb–Pb collisions at $\sqrt{s_{NN}} = 2.76$ TeV are presented. The paper is organised as follows: in Sect. 2 a brief description of the ALICE detector is given and in Sect. 3 the event and track selections used in the present analysis are described. In Sect. 4 the different techniques used to identify deuterons and anti-deuterons are presented, together with the efficiency and acceptance corrections used for the determination of the transverse momentum spectra. In Sect. 5 the technique used to evaluate the deuteron elliptic flow and the obtained results are described, together with the comparison of deuteron and lighter particles elliptic flow. Section 6 is devoted to the comparison of the measured deuteron transverse momentum spectra and elliptic flow with different theoretical models, namely the Blast-Wave model, which is a hydro-based model [13–16], the coalescence model [17] and the dynamic coalescence model implemented in the AMPT generator [18]. Finally, in Sect. 7 the conclusions of this work are presented.

2 The ALICE detector

A detailed description of the ALICE detector can be found in [19] and references therein. For the present analysis the main sub-detectors used are the V0 detector, the Inner Tracking System (ITS), the Time Projection Chamber (TPC), the Time of Flight (TOF) and the High Momentum Particle Identification Detector (HMPID) which are located inside a maximum 0.5 T solenoidal magnetic field. The V0 detector [20] is formed by two arrays of scintillation counters placed around the beampipe on either side of the interaction point: one covering the pseudorapidity range $2.8 < \eta < 5.1$ (V0-A) and the other one covering $-3.7 < \eta < -1.7$ (V0-C). The collision centrality is estimated using the multiplicity measured in the V0 detector as detailed in Sect. 3. The V0 detector is also employed in the elliptic flow measurement as described in Sect. 5.

The ITS [21], designed to provide high resolution track points in the vicinity of the interaction region, is composed of three subsystems of silicon detectors placed around the interaction region with a cylindrical symmetry. The Silicon Pixel Detector (SPD) is the subsystem closest to the beampipe and it is made of two layers of pixel detectors. The third and the fourth layers are formed by Silicon Drift Detectors (SDD), while the outermost two layers are equipped with double-sided Silicon Strip Detectors (SSD). The inner radius of the

SPD, 3.9 cm, is limited by the beampipe, while the TPC defines the radial span of the detector to be 43 cm. The ITS covers the pseudorapidity range $|\eta| < 0.9$ and it is hermetic in azimuth.

The same pseudorapidity range is covered by the TPC [22], which is the main tracking detector, consisting of a hollow cylinder whose axis coincides with the nominal beam axis. The active volume, filled with a gas at atmospheric pressure, has an inner radius of about 85 cm, an outer radius of about 250 cm, and an overall length along the beam direction of 500 cm. The gas is ionised by charged particles traversing the detector and the ionisation electrons drift, under the influence of a constant electric field of ~ 400 V/cm, towards the endplates where their arrival point is measured. The trajectory of a charged particle is estimated using up to 159 combined measurements (clusters) of drift times and radial positions of the ionisation electrons. The charged-particle tracks are then built by combining the hits in the ITS and the reconstructed clusters in the TPC. The tracks are then back-propagated to the beampipe to locate the primary collision position (primary vertex) with a resolution of about 100 μm in the direction transverse to the beams for heavy-ion collisions. The TPC is used for particle identification through the specific energy loss (dE/dx) measurement in the TPC gas.

The TOF system [23] covers the full azimuth for the pseudorapidity interval $|\eta| < 0.9$. The detector is based on the Multi-gap Resistive Plate Chambers (MRPCs) technology and it is located, with a cylindrical symmetry, at an average distance of 380 cm from the beam axis. The particle identification is based on the difference between the measured time-of-flight and its expected value, computed for each mass hypothesis from track momentum and length. The detector time resolution is about 80 ps.

The HMPID detector [19] consists of seven identical Ring Imaging Cherenkov (RICH) modules, in proximity focusing configuration, located at 475 cm from the beam axis. The HMPID, with its surface of about 12 m^2 , covers a limited acceptance of $|\eta| < 0.55$ and $1.2^\circ < \phi < 58.5^\circ$. A HMPID module has three independent radiators, each one consisting of a 15 mm thick layer of liquid C_6F_{14} (perfluorohexane) with a refractive index of $n = 1.289$ at a photon wavelength $\lambda = 1.75$ nm. They are coupled to multi-wire proportional chamber based photon detectors with CsI photocathodes. The HMPID complements the particle identification capabilities provided by the TPC and TOF detectors, extending the p_T reach up to 4 GeV/ c for pions and kaons and up to 6 GeV/ c for protons [24].

3 Data sample

The analyses presented here are based on the data collected in the year 2011. In total, the data sample consists of nearly

40 million Pb–Pb collisions at $\sqrt{s_{\text{NN}}} = 2.76$ TeV after offline event selection. The events are collected using a trigger logic that requires the coincidence of signals on both sides of the V0 detector (V0-A and V0-C). An online selection based on the V0 signal amplitudes is used to enhance the sample of central and semi-central collisions through two separate trigger classes. The scintillator arrays have an intrinsic time resolution better than 0.5 ns, and their timing information is used together with that from the Zero Degree Calorimeters [19] for offline rejection of events produced by the interaction of the beams with residual gas in the vacuum pipe. Furthermore, in the offline selection only events with a reconstructed primary vertex position along the z direction in the fiducial region $|V_z| < 10$ cm are selected.

The V0 detectors are used also to determine the centrality of Pb-Pb collisions. The amplitude distribution of V0 is fitted with a Glauber Monte Carlo to compute the fraction of the hadronic cross section corresponding to a given range of amplitude. From the Glauber Monte Carlo fit it is possible to classify events in several centrality percentiles selecting amplitudes measured in the V0 detectors as it was shown in [25, 26]. The contamination from electromagnetic processes is found to be negligible for the 80% most central events.

The p_T spectra and elliptic flow of primary anti-deuterons and deuterons are measured at mid-rapidity ($|y| < 0.5$). A pseudorapidity selection ($|\eta| < 0.8$) is used in order to analyse only those tracks in the region where ALICE is able to perform full tracking and provide the best particle identification information. Primary particles are those produced in the collision, including all the decay products, except those from weak decays. The main secondary deuteron contribution comes from the knock-out deuterons produced by the interaction of primary particles with the material of the beampipe and of the apparatus. This is relevant for the spectra and elliptic flow measurements for $p_T \leq 1.4$ GeV/c. The only known contribution to secondary deuterons and anti-deuterons from weak decays originates from the charged three-body decay of the hypertriton (${}^3_{\Lambda}\text{H} \rightarrow \text{d} + \text{p} + \pi^-$) and of the anti-hypertriton (${}^3_{\bar{\Lambda}}\text{H} \rightarrow \bar{\text{d}} + \bar{\text{p}} + \pi^+$). From the measurement of the hypertriton production via its charged two-body decay [27] we know that this contribution is negligible.

In order to guarantee a track momentum resolution of 2% in the relevant p_T range and a dE/dx resolution of about 6%, selected tracks are required to have at least 70 clusters in the TPC and two points in the ITS (out of which at least one in the SPD). The distances of closest approach to the primary vertex in the plane perpendicular (DCA_{xy}) and parallel (DCA_z) to the beam axis for the selected tracks are determined with a resolution better than 300 μm [19]. In order to suppress the contribution of secondary particles only tracks with $|\text{DCA}_z| \leq 1$ cm are selected. Moreover, the χ^2 per TPC

cluster is required to be less than 4 and tracks of weak-decay products are rejected as the deuteron is a stable nucleus.

4 Transverse momentum spectra analyses

In this paper we present deuterons spectra obtained at p_T higher than 4.4 GeV/c extending significantly the transverse momentum range covered in the previous ALICE study [2]. As in the previous analysis, the spectra are determined in the centrality ranges 0–10, 10–20 and 20–40% consisting of 16.5, 4.5 and 9 millions of events, respectively. The particle identification is mainly performed by combining the information from the TPC and the TOF detectors, enabling the spectra measurement up to $p_T = 6$ GeV/c. In the 0–10% centrality interval it is also possible to further extend the measurement of the production spectra to $p_T = 8$ GeV/c using the HMPID detector.

4.1 Particle identification

The TPC and TOF combined analysis presented in this paper adopts the same identification strategy used in the previous ALICE measurement of light (anti-)nuclei production [2]. With the large data sample collected in 2011 the deuteron transverse-momentum spectra measurement is extended up to 6 GeV/c. It is required that the measured energy-loss signal of a track as measured in the TPC lies in a 3σ window around the expected value for a given mass hypothesis. In addition, from the measured time-of-flight t of the track, the mass m of the corresponding particle can be obtained as:

$$m^2 = \frac{p^2}{c^2} \cdot \left(\frac{c^2 t^2}{L^2} - 1 \right). \quad (3)$$

The total momentum p and the track length L are determined using the tracking detectors.

The $m^2 - m_{\text{PDG}}^2$ distribution, where m_{PDG} is the nominal mass of deuteron as reported in [28], is measured for all p_T intervals up to 6 GeV/c and it is fitted with a Gaussian function with an exponential tail. This is necessary to describe the asymmetric response of TOF. The background has two main components: the wrong association of a track with a TOF cluster and the exponential tail of lower mass particles. For this reason the background is modelled using the sum of two exponential functions. An example of the fit used to extract the deuteron yield in the $4.4 \leq p_T < 5$ GeV/c interval for the 0–10% centrality range is shown in the left panel of Fig. 1.

The TPC and TOF combined analysis is extended by using the HMPID measurement. With the available statistics and due to the limited geometrical acceptance of the HMPID only results in the 0–10% central Pb-Pb collisions are extracted.

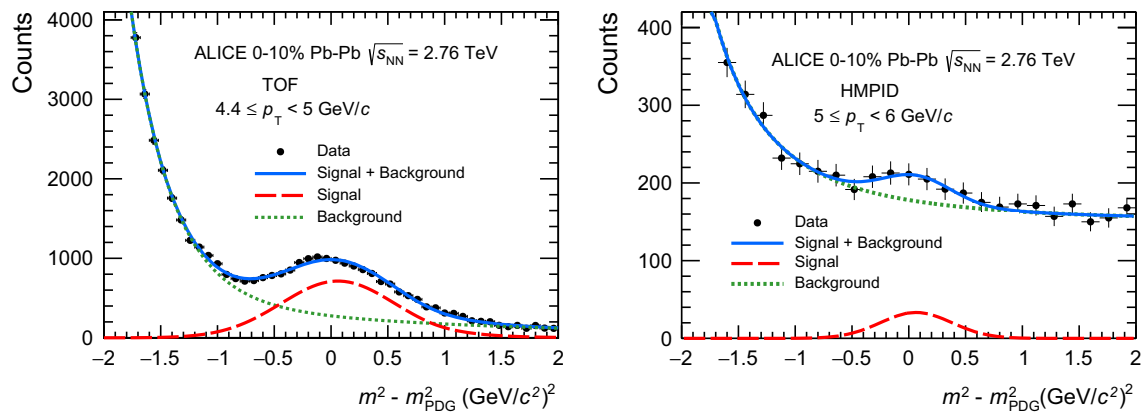


Fig. 1 The $m^2 - m_{\text{PDG}}^2$ distributions obtained using the TOF detector (left) and with the HMPID detector (right) in two different p_T intervals ($4.4 \leq p_T < 5$ GeV/c and $5 \leq p_T < 6$ GeV/c) for positive tracks in the 0–10% centrality class. Here m_{PDG} is the nominal mass

The event and track selections are similar to those of the combined TPC and TOF analysis, but in addition it is required that the track is propagated to the charged-particle cluster in the MWPC of the HMPID. A maximal distance of 5 cm between the centroid of the charged-particle cluster and the track extrapolation on the cathode plane is required to reject the fake associations in the detector. This selection, tuned via Monte Carlo simulations, represents the best compromise between loss of statistics and the probability of a correct association. The particle identification in the HMPID detector is based on the measurement of the Cherenkov angle (θ_{Ckov}) which allows us to determine the square mass of the particle by the following formula:

$$m^2 = p^2 \cdot (n^2 \cos^2 \theta_{\text{Ckov}} - 1), \quad (4)$$

where n is the refractive index of the liquid radiator (C_6F_{14} with $n = 1.29$ at temperature $T = 20$ °C for photons with an energy of 6.68 eV) and p is the momentum of the track.

In the 0–10% centrality class, where the total number of hits in the HMPID chambers is large, the reconstruction of the Cherenkov angle is also due to photons that are not associated to the particle. These wrong photon associations reduce the particle identification efficiency and similar effects are observed in the Monte Carlo simulations. The response function is a Gaussian distribution for correctly assigned rings and the raw yields are extracted by using an unfolding technique. The background mainly originates from fake photon associations and it is described with a second degree polynomial plus a $1/x^4$ term. Signal and background shapes are tuned via Monte Carlo simulations, as done for lighter mass particles [24].

An example of the distribution of the mass squared measured with the HMPID detector in the p_T interval $5 \leq p_T < 6$ GeV/c for positive tracks in the 0–10% centrality interval

of deuteron as reported in [28]. Solid lines represent the total fit (signal plus background), dotted lines correspond to background and dashed lines to deuterons signal

is shown in the right part of Fig. 1. Solid lines represent the total fit (signal plus background); dotted lines correspond to the background and dashed lines to deuterons signal.

4.2 Corrections

The final p_T spectra of (anti-)deuterons are obtained by correcting the raw spectra for the tracking efficiency and geometrical acceptance. The correction is defined in the same way for the two PID techniques (i.e. TPC–TOF and HMPID) and it is computed as the ratio of the number of detected particles to the number of generated particles within the relevant phase space. The HIJING event generator [29] is used to generate background events. To these deuterons and anti-deuterons are explicitly added with a flat distribution both in transverse momentum and in azimuth. The GEANT3 transport code [30] is used to transport the tracks of the particles through the ALICE detector geometry. GEANT3 includes a limited simulation of the interaction of deuterons and anti-deuterons with the material because of the lack of experimental data on collisions of light nuclei with the different materials. For the present study, GEANT3 was modified as discussed in [2]: the cross-section of anti-nuclei are approximated in a simplified empirical model by a combination of the anti-proton ($\sigma_{\bar{p}A}$) and anti-neutron ($\sigma_{\bar{n}A}$) cross sections, following the approach presented in [31]. A full detector simulation with GEANT4 (v10.01) [32] has been performed in order to cross check the tracking efficiency estimation performed with the modified GEANT3. Since there was a dedicated effort in the GEANT4 code to interpolate the available measurements of the cross section of interaction between anti-nuclei and nuclei [33], the correction for the interaction of (anti-)deuterons with the detector material from GEANT3 is scaled to match the expected value from GEANT4. Half of

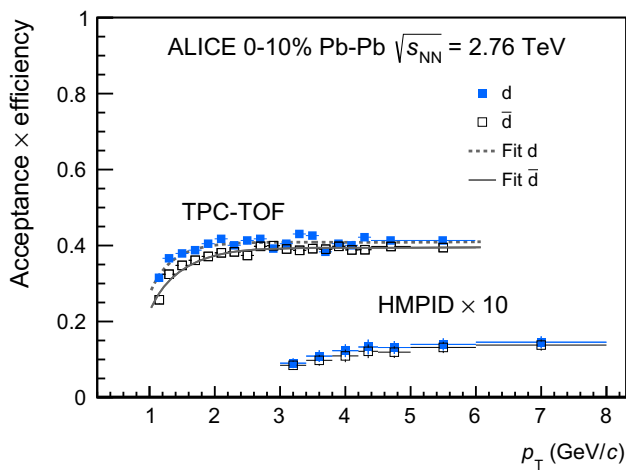


Fig. 2 Acceptance \times efficiency ($A \times \varepsilon$) as a function of transverse momentum for deuterons (filled markers) and anti-deuterons (open markers) in the most 10% central Pb–Pb collisions at $\sqrt{s_{NN}} = 2.76$ TeV for TPC-TOF and HMPID (multiplied by a scaling factor) analyses. The TPC-TOF points account for tracking, matching efficiency and geometrical acceptance. The dashed and solid curves represent the fits with the function presented in Eq. 5 for deuterons and anti-deuterons respectively (see text for details). The HMPID points take into account tracking efficiency, geometrical acceptance, $\varepsilon_{\text{dist}}$ (“distance correction factor” as explained in the text) and PID efficiency. The lower value with respect to the TPC-TOF is mainly due to the limited geometrical acceptance of the HMPID detector (5%)

the difference between the efficiencies evaluated with the two codes is 8% for deuteron tracks matched to the TOF, while it is 10% for anti-deuterons tracks. This difference is taken into account in the systematic uncertainties of the production spectra of deuterons and anti-deuterons. The requirement of a TOF hit matched to the track reduces the overall efficiency to about 40% in the p_T region of interest, mainly due to the TOF geometrical acceptance and to the material.

Figure 2 shows the product of acceptance and efficiency ($A \times \varepsilon$) for (anti-)deuterons as a function of p_T . The TPC and TOF $A \times \varepsilon$ (open points) accounts for tracking efficiency, geometrical acceptance and matching efficiency. The dashed line represents a fit with the ad-hoc functional form

$$f(p_T) = a_0 + a_1 e^{a_2 \cdot p_T} + a_3/p_T + a_4/(p_T)^2, \quad (5)$$

where a_0, a_1, a_2 and a_3 are free parameters. This fit function is used to smooth the fluctuations in the $A \times \varepsilon$ correction. However, correcting the raw spectra with either the fit function or the binned values leads to negligible differences with respect to the total systematic uncertainties. The HMPID raw spectra are corrected for tracking efficiency and geometrical acceptance as it has been done for the TPC and TOF combined analysis, but the correction is higher mainly due to the limited geometrical acceptance of the HMPID detector. The HMPID particle identification efficiency is related to the Cherenkov angle reconstruction efficiency. It is computed by

means of Monte Carlo simulations that reproduce the background observed in the data and it is defined as the ratio of the identified deuteron signal to the generated deuteron signal in the HMPID chambers. It reaches 50% for (anti-)deuterons at higher transverse momenta. A data-driven cross check of the efficiency at lower p_T is performed using a clean sample of (anti-)deuterons defined within 2σ of the expected values measured by the TOF detector, showing excellent compatibility – within statistical uncertainties – between the two methods. In Fig. 2, the convolution of tracking efficiency, geometrical acceptance, distance correction factor ($\varepsilon_{\text{dist}}$) and PID efficiency for the HMPID analysis in Pb–Pb collisions at $\sqrt{s_{NN}} = 2.76$ TeV in 0–10% centrality collisions is also shown.

The track-fitting algorithm in ALICE takes into account the Coulomb scattering and energy loss using the mass hypothesis of the pion. The energy loss of heavier particles, such as the deuterons, is considerably higher than the energy loss of pions, therefore a track-by-track correction is necessary. This correction is obtained from the difference between the generated and the reconstructed momentum in a full Monte Carlo simulation of the ALICE detector. As already discussed in [2], the effect of this correction is negligible for high p_T deuterons. This momentum correction was included in systematics checks for the elliptic flow determination and its effect was found to be negligible.

4.3 Systematic uncertainties and results

The systematic uncertainties for the two spectra analyses mainly consist of three components, in order of relevance:

- transport code: the uncertainty on the hadronic cross section of the (anti-)deuterons with the material, estimated taking the difference between the efficiencies evaluated with GEANT3 and GEANT4;
- the fitting uncertainties for the signal extraction, studied by changing the functional form of the fitting function. The uncertainty has been estimated computing the RMS of the results of these variations;
- the track selection bias assessed through the variation of the track selection criteria. Among the probed selections there are the PID fiducial cut in the TPC and the track DCA_z selection, whose variations turned into a negligible contribution ($\leq 1\%$) to the systematic uncertainties. Since the effects of the variation of the DCA_z selection are negligible, we can conclude that the production spectra of deuterons are not affected by secondary particles originating from material in the high p_T region.

The other contributions to the systematic uncertainties are related to the limited knowledge of the material budget, the PID and the $\varepsilon_{\text{dist}}$ correction for the HMPID analysis. Table 1

Table 1 Details of the systematic uncertainties assigned in the TPC and TOF combined and HMPID analyses. The values in the parentheses refer to the systematic for the anti-deuteron spectra when different to the deuteron ones

p_T interval (GeV/c)	TPC-TOF		HMPID	
	4.4–5.0 (%)	5.0–6.0 (%)	5.0–6.0 (%)	6.0–8.0 (%)
Transport code	8 (10)		8 (10)	
Signal extraction	3	3	13 (15)	15 (18)
Track selection	7	7	6	7
Material budget	3		3	
HMPID $\varepsilon_{\text{dist}}$	–		5	
HMPID PID	–		4	

illustrates the details about the systematic uncertainties for the spectra analyses in each p_T interval presented in this paper.

The results of the two analyses in the 0–10% centrality interval and in the p_T range between 5 and 6 GeV/c are compatible within the uncertainties, thus in the final spectra they are combined using a weighting procedure. The weights used in the combination are the uncorrelated systematic uncertainties, given that the statistical uncertainties of the two analyses are partially correlated. The resulting spectra are shown in the upper panel of Fig. 3 for $p_T > 4.4$ GeV/c. For lower transverse momenta, as the data sample used for the analyses at high p_T presented in this paper was collected with a larger coverage of the Transition Radiation Detector and a lower performance of the Silicon Pixel Detector, the spectra extracted in [2] have smaller systematic uncertainties and they are used in Fig. 3. The spectra extracted with the two data samples are compatible within the systematic uncertainties.

The bottom panels of Fig. 3 show the ratios between the deuteron and anti-deuteron spectra for the different centrality classes as a function of the transverse momentum. As already observed in [2] and predicted by coalescence and thermal models the ratio is compatible with unity over the full transverse momentum region. The integrated yield and the mean transverse momentum are extracted by fitting the spectra in each centrality interval with the Blast-Wave function [34] and they are in agreement within the experimental uncertainties with the values shown in [2].

5 Elliptic flow measurements

5.1 Analysis technique

The determination of the deuteron elliptic flow is performed over the same sample of Pb–Pb collisions at $\sqrt{s_{\text{NN}}} = 2.76$ TeV as already described in Sect. 3, and the full event sample is divided into 6 different centrality intervals (0–5%, 5–10%,

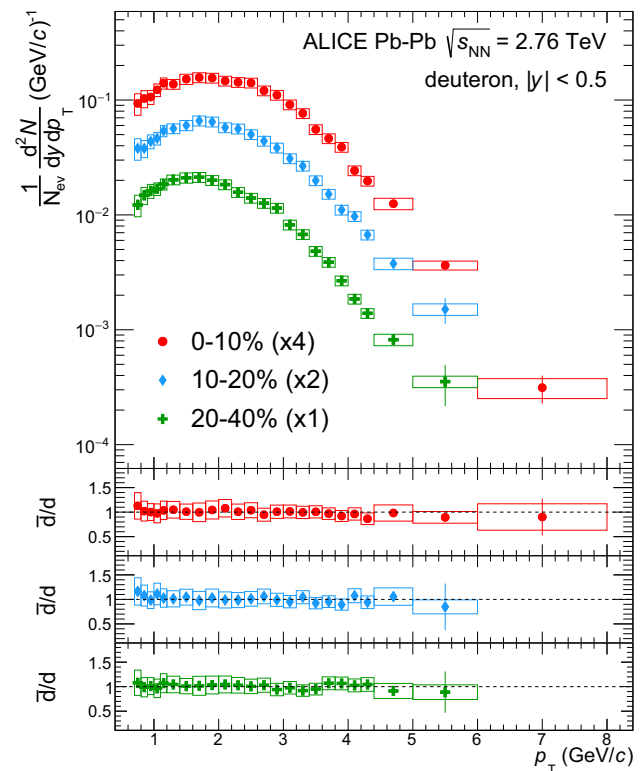


Fig. 3 In the upper panel the deuteron p_T spectra are shown for the three centrality intervals extended to high p_T with the TOF and HMPID analyses. In the lower panels the ratios of anti-deuterons and deuterons are shown for the 0–10%, 10–20% and 20–40% centrality intervals, from top to bottom. The ratios are consistent with unity over the whole p_T range covered by the presented analyses

10–20%, 20–30%, 30–40% and 40–50%). The identification of deuterons (d) and anti-deuterons (\bar{d}) is performed in the $0.8 < p_T < 5$ GeV/c transverse momentum interval as follows: for momenta up to 1.4 GeV/c the energy loss in the TPC gives a clean sample of (anti-)deuterons by requiring a maximum deviation of the specific energy loss of 3σ with respect to the expected signal; above 1.4 GeV/c a hit on the TOF detector is required, similarly to what has been described in the Sect. 4.1. In order to increase the statistics, deuterons and anti-deuterons are combined ($d+\bar{d}$) for all the centrality intervals and in the transverse-momentum interval $p_T > 1.4$ GeV/c. This is possible since the results for the two separated particles are compatible within statistical uncertainties. For lower momenta ($0.8 \leq p_T < 1.4$ GeV/c) only anti-deuterons are used to avoid effects related to secondary deuterons created through the interaction of particles with the material. The $d+\bar{d}$ signal in the TOF detector is fitted with a Gaussian with an exponential tail, while the background is fitted with an exponential. An example of the ΔM distribution, where $\Delta M = m - m_{\text{PDG}}$, for deuterons plus anti-deuterons with $2.20 \leq p_T < 2.40$ GeV/c and centrality interval 30–40% is shown in the left part of Fig. 4.

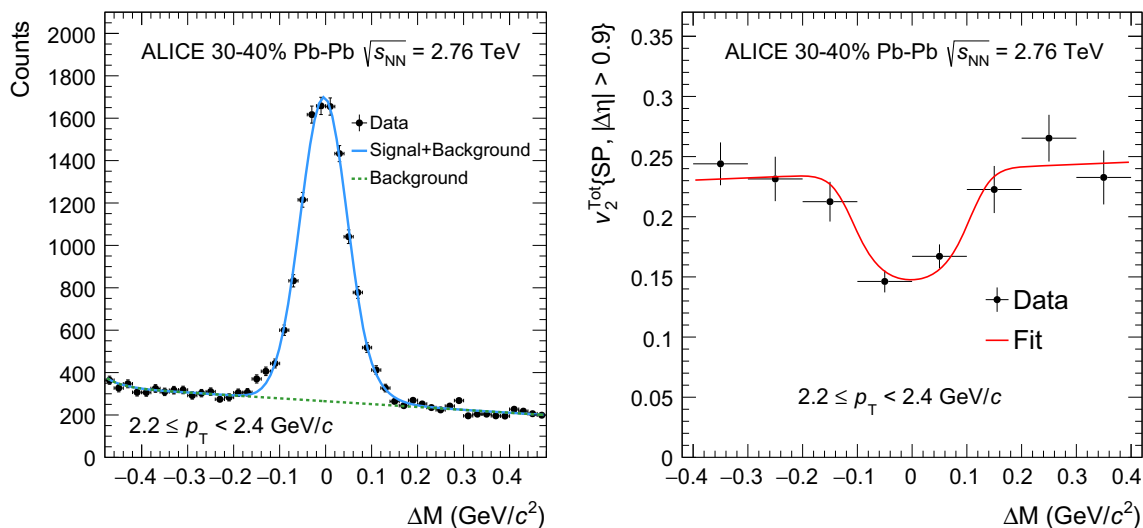


Fig. 4 Left: Distribution of ΔM for $d+\bar{d}$ in the $2.2 \leq p_T < 2.4$ GeV/c and centrality interval 30–40% fitted with a Gaussian with an exponential used to reproduce the signal and an exponential to reproduce the

background. Right: The v_2^{Tot} vs ΔM for $d+\bar{d}$ for $2.2 \leq p_T < 2.4$ GeV/c in events with 30–40% centrality. Points represent the measured v_2^{Tot} , while the curve is the fit performed using Eq. 7

The v_2 coefficient is measured using the Scalar Product (SP) method [7, 35], a two-particle correlation technique, using a pseudo-rapidity gap $|\Delta\eta| > 0.9$ between the identified hadron under study and the reference flow particles. The applied gap reduces the non-flow effects (e.g. jets), which are correlations not arising from a collective motion. The results presented in this paper are obtained by dividing each event into three sub-events A, B and C, using three different pseudo-rapidity regions. The reference particles were taken from sub-events A and C, using the V0-A ($2.8 < \eta < 5.1$) and V0-C ($-3.7 < \eta < -1.7$) detectors, respectively, while deuterons were taken from sub-events B within $|\eta| < 0.8$. The v_2 coefficient was then calculated as described in [35]

$$v_2 = \sqrt{\frac{\left\langle \left\langle \vec{u}_2^B \cdot \frac{\vec{Q}_2^{A*}}{M_A} \right\rangle \left\langle \vec{u}_2^B \cdot \frac{\vec{Q}_2^{C*}}{M_C} \right\rangle \right\rangle}{\left\langle \frac{\vec{Q}_2^A}{M_A} \cdot \frac{\vec{Q}_2^{C*}}{M_C} \right\rangle}}, \tag{6}$$

where the two brackets in the numerator indicate an average over all the particles of interest and over all the events, M_A and M_C are the estimates of multiplicity from the V0-A and V0-C detectors, and \vec{Q}_2^{A*} , \vec{Q}_2^{C*} are the complex conjugates of the flow vector [36] calculated in sub-event A and C, respectively, and \vec{u}_2^B is the unit flow vector measured in sub-event B. The contribution to the measured elliptic flow (v_2^{Tot}) due to misidentified deuterons (v_2^{Bkg}) is removed by studying the azimuthal correlations versus ΔM . This method is based on the observation that, since v_2 is additive, candidates v_2^{Tot} can be expressed as a sum of signal ($v_2^{\text{Sig}}(\Delta M)$) and background ($v_2^{\text{Bkg}}(\Delta M)$) weighted by their relative yields

$$v_2^{\text{Tot}}(\Delta M) = v_2^{\text{Sig}}(\Delta M) \frac{N^{\text{Sig}}}{N^{\text{Tot}}}(\Delta M) + v_2^{\text{Bkg}}(\Delta M) \frac{N^{\text{Bkg}}}{N^{\text{Tot}}}(\Delta M), \tag{7}$$

where N^{Tot} is the total number of candidates, N^{Bkg} and $N^{\text{Sig}} = N^{\text{Tot}} - N^{\text{Bkg}}$ are the numbers of background and signal for a given mass and p_T interval. The yields N^{Sig} and N^{Bkg} are extracted from fits to the ΔM distributions obtained with the TOF detector for each centrality and p_T interval. The v_2^{Tot} vs ΔM for $d+\bar{d}$ for $2.2 \leq p_T < 2.4$ GeV/c in events with 30–40% centrality is shown in the right panel of Fig. 4, where the points represent the measured v_2^{Tot} and the curve is the fit performed using Eq. 7. The v_2^{Bkg} was parametrized as a first-order polynomial ($v_2^{\text{Bkg}}(\Delta M) = p_0 + p_1 \Delta M$).

5.2 Systematic uncertainties and results

The systematic uncertainties are determined by varying the event and track selections. The contribution of each source is estimated, for each centrality interval, as the root mean square deviation of the $v_2(p_T)$ extracted from the variations of the cut values relative to the results described above. The total systematic uncertainty was calculated as the quadratic sum of each individual contribution. The event sample is varied by changing the cut on the position of the primary vertex along the beam axis from ± 10 to ± 7 cm, by replacing the centrality selection criteria from the amplitude of the signal of the V0 detector to the multiplicity of the TPC tracks and by separating runs with positive and negative polarities

Table 2 Summary of the systematic uncertainties for the determination of the deuterons v_2 coefficient

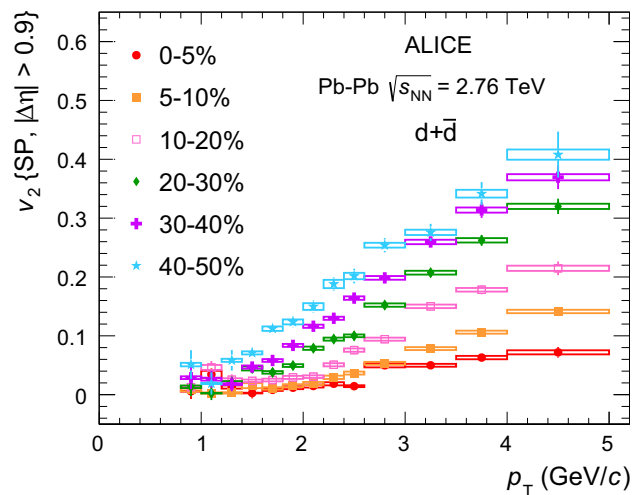
Source	Value
Event Selections	< 1%
Particle Identification	2%
Fit to v_2^{Tot} vs ΔM	3%
TPC and TOF occupancy (absolute value)	0.02 (TPC) 0.01 (TOF)

of the solenoidal magnetic field. The systematic uncertainties related to these changes are found to be smaller than 1%. Additionally, systematic uncertainties related to particle identification are studied by varying the number of standard deviations around the energy loss expected for deuterons in the TPC and, similarly, for the time of flight in the TOF detector and by varying the distance of closest approach in the DCA_{xy} of accepted tracks. These contributions are found to be around 2% for all the measured transverse-momentum and centrality intervals. The systematic uncertainties originating from the determination of N^{Sig} , N^{Tot} and N^{Bkg} in Eq. 7, are studied by using different functions to describe the signal and the background. The function adopted to describe the $v_2^{\text{Bkg}}(\Delta M)$ is varied using different polynomials of different orders. The contribution to the final systematic uncertainties is found to be around 3% for all the analysed transverse-momentum and centrality intervals. The main contributions to the systematic uncertainties of deuteron elliptic flow are related to TPC and TOF occupancy [35]. These contributions were studied in detail in [35] and are adopted in the present analysis, leading to absolute systematic uncertainties of 0.02 and 0.01 related to TPC and TOF occupancy, respectively. A summary of all the systematic uncertainties can be found in Table 2.

The measured v_2 as a function of p_T for $d+\bar{d}$ is shown in Fig. 5. Each set of points corresponds to a different centrality class: 0–5, 5–10, 10–20, 20–30, 30–40 and 40–50%, as reported in the legend. Vertical lines represent statistical errors, while boxes are systematic uncertainties. The value of $v_2(p_T)$ increases progressively from central to semi-central collisions. This behaviour is consistent with the picture of the final-state anisotropy driven by the collision geometry, as represented by the initial-state eccentricity which decreases from peripheral to central collisions.

5.3 Comparison with other identified particles and test of scaling properties

In order to study the spectra and the elliptic flow of deuterons simultaneously, the latter has been determined in the same centrality intervals selected for the p_T spectra (0–10, 10–20 and 20–40%) (see Sect. 4). The measured v_2 coefficient for $d+\bar{d}$ is compared with that of pions and protons [35]. The

**Fig. 5** Measured v_2 as a function of p_T for \bar{d} ($p_T < 1.4$ GeV/c) and $d+\bar{d}$ ($p_T \geq 1.4$ GeV/c) for different centrality intervals in Pb–Pb collisions at $\sqrt{s_{\text{NN}}} = 2.76$ TeV. Vertical bars represent statistical errors, while boxes are systematic uncertainties

results in the 20–40% centrality interval are shown in Fig. 6. The v_2 of π^\pm (empty circles), $p+\bar{p}$ (filled squares) and $d+\bar{d}$ (filled circles) as a function of p_T are shown in the top left panel of the figure. It is observed that at low p_T deuterons follow the mass ordering observed for lighter particles, which is attributed to the interplay between elliptic and radial flow [15, 37]. The second column of Fig. 6 is used to test the scaling properties of v_2 with the number of constituent quarks (n_q). It has been observed at RHIC [38–40] that the various identified hadron species approximately show a follow a common behaviour [41], while nuclei follow an atomic mass number scaling in the $0.3 < p_T < 3$ GeV/c interval [5]. The v_2 coefficient divided by n_q is shown as a function of p_T/n_q in the upper panel: the experimental data indicate only an approximate scaling at the LHC energy for deuterons. To quantify the deviation, the p_T/n_q dependence of v_2/n_q for protons and anti-protons is fitted with a seventh-order-polynomial function and the ratio of $(v_2/n_q)/(v_2/n_q)_{\text{Fit p}}$ is calculated for each particle. A deviation from the n_q scaling of the order of 20% for $p_T/n_q > 0.6$ is observed for deuterons; the same behaviour is observed in the other centrality intervals (not shown). Finally, in the third column, the measured v_2/n_q is shown as a function of the transverse kinetic energy scaled by the number of constituent quarks $(KE_T)/n_q = (m_T - m_0)/n_q$ of each particle. This scaling, introduced by the PHENIX collaboration [42] for low p_T , was initially observed to work well – within statistical uncertainties – at RHIC energies in central A–A collisions [38, 41]. However, recent publications report deviations from this scaling for non central Au–Au collisions [43]. Also at the LHC energy the proposed scaling does not work properly (deviations up to $\sim 20\%$) [35], and the scaling is not valid for

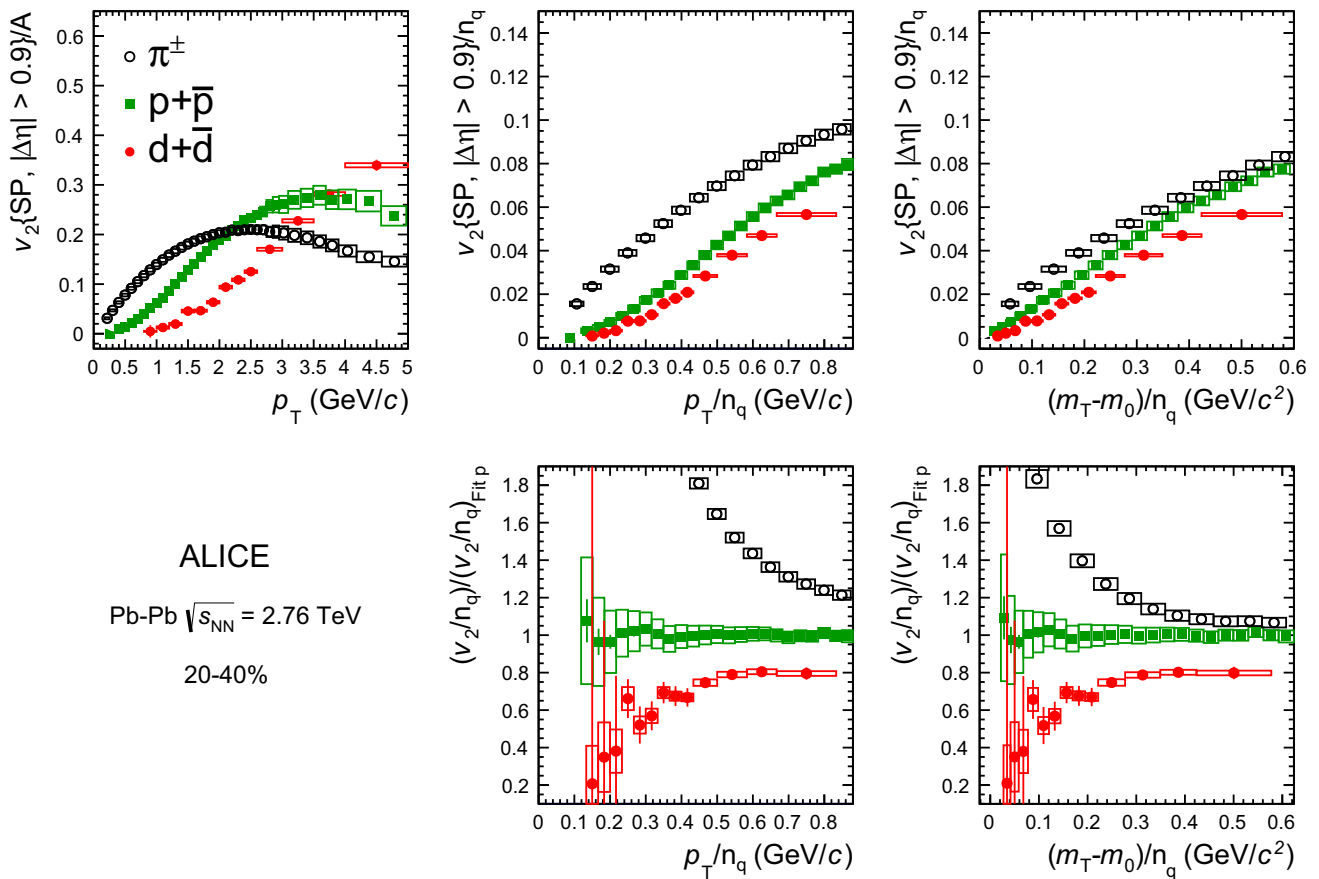


Fig. 6 v_2 of π^\pm (empty circles), $p+\bar{p}$ (filled squares) and $d+\bar{d}$ (filled circles) measured in the 20–40% centrality interval. A detailed description of each panel can be found in the text

deuterons either. The deviations are quantified in the bottom panel, where the ratio of $(v_2/n_q)/(v_2/n_q)_{Fit\ p}$ for each particle is shown. Significant deviations are found for $KE_T/n_q < 0.3$ GeV/c, indicating that also for light nuclei the scaling with n_q does not hold at the LHC energy. For $KE_T/n_q > 0.3$ GeV/c, data exhibit deviations from an exact scaling at the level of 20%.

6 Comparison with different theoretical models

6.1 Comparison with Blast-Wave model

The nuclear fireball model was introduced in 1976 to explain midrapidity proton-inclusive spectra [13]. This model assumes that a clean cylindrical cut is made by the projectile and target leaving a hot source in between them. Protons emitted from this fireball should follow a thermal energy distribution, and are expected to be emitted isotropically. Such a model, called Blast-Wave model, has evolved since then, with more parameters to describe both the p_T spectra and the anisotropic flow of produced particles [14–16]. As described in [15], the transverse mass spectrum can be expressed as

$$\frac{dN}{dy dm_T^2 d\phi_p} \sim \int_0^{2\pi} d\phi_s K_1(\beta_t(\phi_s)) e^{\alpha_t(\phi_s) \cos(\phi_s - \phi_p)}, \quad (8)$$

where ϕ_s and ϕ_p are the azimuthal angles in coordinate and momentum space; the arguments $\alpha_t(\phi_s) = (p_T/T) \sinh(\rho(\phi_s))$ and $\beta_t(\phi_s) = (m_T/T) \cosh(\rho(\phi_s))$ are based on a ϕ_s -dependent radial flow rapidity $\rho(\phi_s)$ and K_1 is a modified Bessel function of the second kind.

The elliptic flow coefficient v_2 is obtained by taking the azimuthal average over $\cos(2\phi_p)$ with this spectrum, $v_2 = \langle \cos(2\phi_p) \rangle$. The integral on ϕ_p can be evaluated analytically

$$v_2(p_T) = \frac{\int_0^{2\pi} d\phi_s \cos(2\phi_s) I_2(\alpha_t(\phi_s)) K_1(\beta_t(\phi_s))}{\int_0^{2\pi} d\phi_s I_0(\alpha_t(\phi_s)) K_1(\beta_t(\phi_s))}, \quad (9)$$

where I_0 and I_2 are modified Bessel functions of the first kind. However, the Blast-Wave fit matched data even better after the STAR Collaboration added a fourth parameter, s_2 , [16] which takes into account the anisotropic shape of the source in coordinate space. With the introduction of the s_2 parameter, the elliptic flow can be expressed as

Table 3 Blast-Wave parameters computed by fitting the pion, kaon and proton transverse-momentum spectra and elliptic flow. See the text for more details

Fit parameters	Centrality classes		
	0–10%	10–20%	20–40%
T (MeV)	96 ± 3	97 ± 2	100 ± 2
$s_2 \times 10^{-2}$	3.21 ± 0.08	6.18 ± 0.11	8.97 ± 0.17
$\rho_0 \times 10^{-1}$	8.2 ± 0.12	8.18 ± 0.10	7.99 ± 0.12
$\rho_a \times 10^{-2}$	1.21 ± 0.05	2.25 ± 0.08	3.09 ± 0.11

$$v_2(p_T) = \frac{\int_0^{2\pi} d\phi_s \cos(2\phi_s) I_2[\alpha_t(\phi_s)] K_1[\beta_t(\phi_s)] [1 + 2s_2 \cos(2\phi_s)]}{\int_0^{2\pi} d\phi_s I_0[\alpha_t(\phi_s)] K_1[\beta_t(\phi_s)] [1 + 2s_2 \cos(2\phi_s)]}, \quad (10)$$

where the masses for different particle species only enter via m_T in $\beta_t(\phi_s)$. The measured pions, kaons and protons p_T spectra [44] and $v_2(p_T)$ [35] are fitted simultaneously using the masses of the different particle species as fixed parameters. The parameters extracted from the fit were used to predict deuteron $v_2(p_T)$ and p_T spectra and are shown in Table 3. The four parameters, as described in [16], represent the kinetic freeze-out temperature (T), the mean transverse expansion rapidity (ρ_0), the amplitude of its azimuthal variation (ρ_a) and the variation the azimuthal density of the source (s_2), respectively.

The simultaneous fit to p_T spectra and $v_2(p_T)$ and the predictions for deuterons are shown in Fig. 7; the centrality decreases going from the left to the right. In the upper part of Fig. 7 the p_T spectra, as well as the ratio between data and model for different centrality intervals, are shown, while the bottom part of the Fig. 7 shows the $v_2(p_T)$ and the ratio between data and model for several centrality intervals. The transverse momentum intervals where the different particle species were fitted are [0.5–1] GeV/ c for pions, [0.2–1.2] GeV/ c for kaons and [0.3–1.7] GeV/ c for protons. These ranges were chosen to be similar to what shown in [2] and to be able to fit at the same time transverse-momentum spectra and v_2 distributions. As can be observed in Fig. 7, the combined fit gives a good description of the deuterons $v_2(p_T)$ within the statistical uncertainties for all measured transverse momenta and centralities. This is in contrast to what has been observed by the STAR experiment in Au–Au collisions at $\sqrt{s_{NN}} = 200$ GeV [5], where the Blast-Wave model underestimates the deuteron v_2 measured in data. Deuteron spectra are underestimated at low p_T (deviations up to 2σ for p_T smaller than 1.8 GeV/ c), while the model is able to reproduce the measured data within 1σ for p_T up to 6 GeV/ c .

6.2 Comparison with coalescence model

Light nuclei have nucleons as constituents and it has been supposed that they are likely to be formed via coalescence of

protons and neutrons which are close in space and have similar velocities. In this production mechanism, the cross section for the production of a cluster with mass number A is related to the probability that A nucleons have relative momenta less than p_0 , which is a free parameter of the model [17]. This provides the following relation between the production rate of the nuclear cluster emitted with a momentum p_A and the nucleons emitted with a momentum p_p

$$E_A \frac{d^3 N_A}{dp_A^3} = B_A \left(E_p \frac{d^3 N_p}{dp_p^3} \right)^A, \quad (11)$$

where $p_A = A p_p$. For a given nucleus, if the spin factors are neglected, the coalescence parameter B_A does not depend on the momentum since it depends only on the cluster parameters

$$B_A = \left(\frac{4\pi}{3} p_0^3 \right)^{(A-1)} \frac{1}{A!} \frac{M}{m^A}, \quad (12)$$

where p_0 is commonly named coalescence radius while M and m are the nucleus and the nucleon mass, respectively. The left panel of Fig. 8 shows the obtained B_2 values for deuterons in three different centrality regions studied in the present work. The measured B_2 values are plotted versus the transverse momentum per nucleon (p_T/A). A clear decrease of the B_2 parameter with increasing centrality and an increase with transverse momentum is observed. The measured B_2 at higher p_T bins presented in this paper follow the trend already observed for smaller momenta, confirming that the experimental result is in contrast to the expectations of the simplest coalescence model [17], where the B_2 is expected to be flat. As already observed in [2], the observed behaviour can be qualitatively explained by position-momentum correlations which are caused by a radially expanding source [45], but better theoretical calculations at the LHC energies are needed.

Since elliptic flow is additive, it is possible to infer the expected v_2 of a composite state (like a deuteron) formed via coalescence starting from Eq. 11. In the region where the coalescence occurs, the elliptic flow of a nucleus can be expressed as a function of the elliptic flow of its constituent nucleons. For a deuteron, assuming that protons and neutrons behave in the same way, the following relation is expected [46]:

$$v_{2,d}(p_T) = \frac{2v_{2,p}(p_T/2)}{1 + 2v_{2,p}^2(p_T/2)}. \quad (13)$$

It is then possible to obtain the expected deuteron elliptic flow starting from the one measured for protons [35]. The results for different centrality intervals are shown in the right part of Fig. 8, where the measured elliptic flow (markers) is compared with simple coalescence predictions (shaded bands) from Eq. 13 for the three different centrality inter-

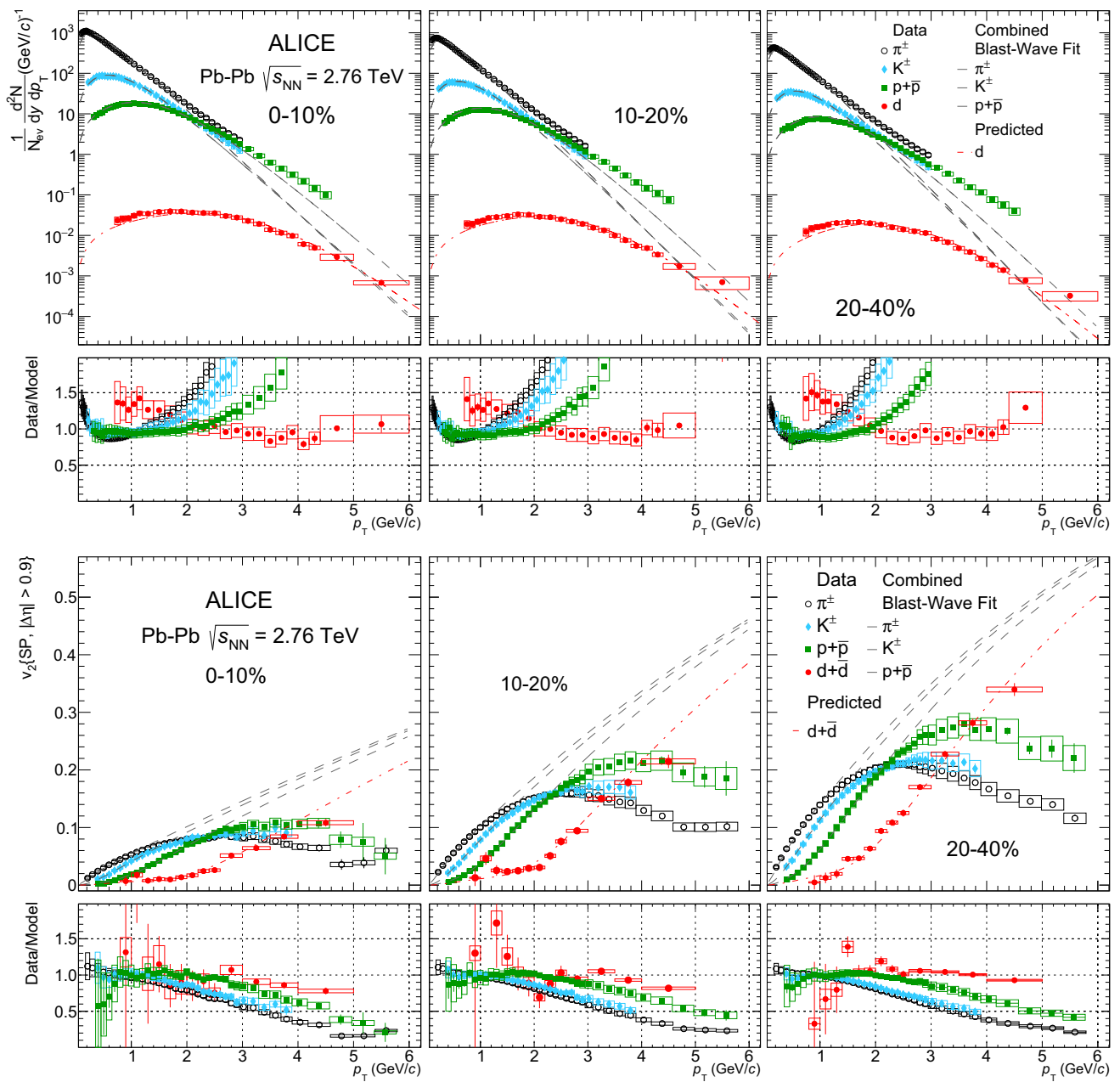


Fig. 7 Combined Blast-Wave fit to p_T and $v_2(p_T)$ distributions using Eqs. 8 and 10. The six upper panels show the p_T spectra and the ratio between data and fit, while the six panels in the bottom part shows the $v_2(p_T)$ and the ratio between data and fit. In each panel, π^\pm (empty circles), K^\pm (diamonds), $p+\bar{p}$ (filled squares) and $d+\bar{d}$ (filled circles) are

shown. For π^\pm , K^\pm and $p+\bar{p}$ the long dashed curves represent the combined p_T and v_2 Blast-Wave fit. Deuteron curves (dash dotted lines) are predictions from lighter particles Blast-Wave combined fit. Each column shows a different centrality intervals (0–10% left, 10–20% middle and 20–40% right)

vals presented in the paper. Also here the simple coalescence is not able to reproduce the measured elliptic flow of deuterons. This behaviour is different with respect to what has been observed at lower energies, where an atomic mass number scaling was observed in the $0.3 < p_T < 3$ GeV/c interval [5]. Improved versions of the coalescence model, for instance based on a realistic phase space distribution of the

constituent protons and neutrons, might describe the elliptic flow of deuterons at LHC energy better.

6.3 Comparison with AMPT

The AMPT model is a hybrid model [18] with the initial particle distributions generated with HIJING [29]. In the default

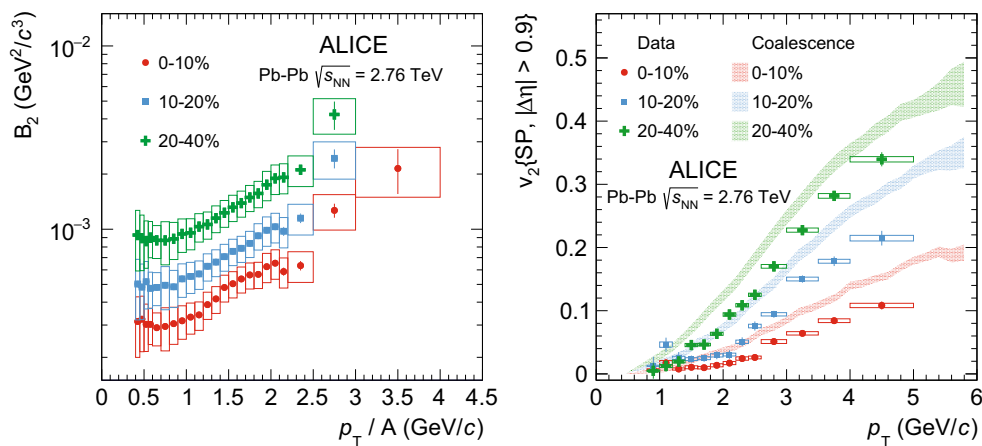


Fig. 8 Left: Coalescence parameter B_2 as a function of the transverse momentum per nucleon (p_T/A) for different centrality classes. Right: Measured v_2 of $d+\bar{d}$ compared with the expectations from simple coalescence (Eq. 13) for different centrality intervals as indicated in the legend

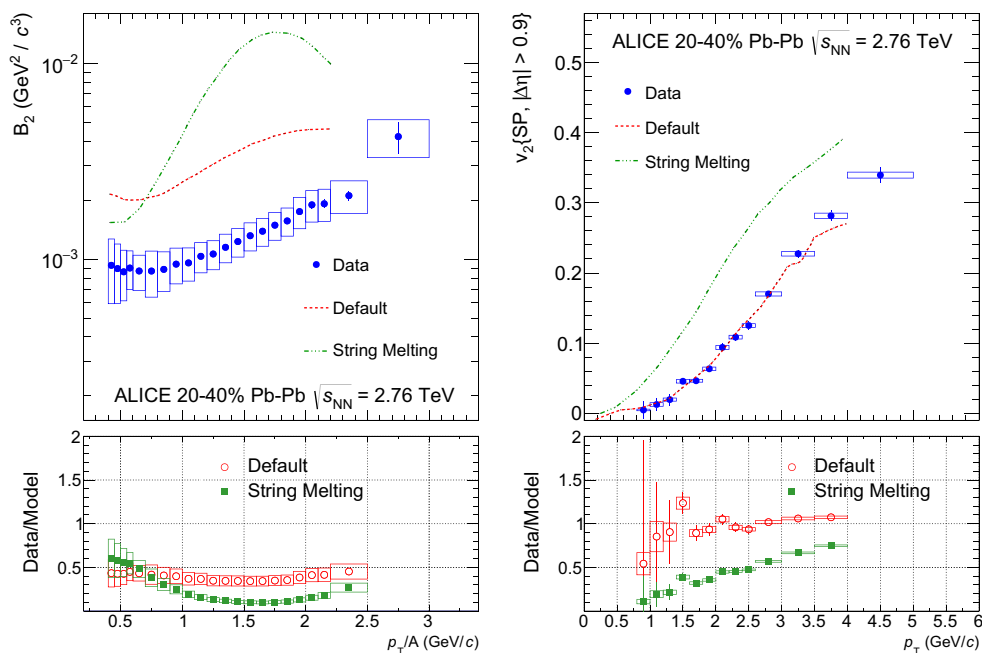


Fig. 9 Measured deuteron (filled dots) B_2 as a function of the transverse momentum per nucleon (p_T/A) (top left panel) and $v_2(p_T)$ parameter (top right panel) compared to those produced with two versions of

the AMPT model (dashed and dotted lines). In the bottom panels, the ratios between the measured data and the expectations from the two models are shown

version of AMPT, the jet quenching in HIJING is replaced by explicitly taking into account the scattering of mini-jet partons via the Zhang's parton cascade (ZPC) model [47]. In the version with string melting, all the hadrons produced from the string fragmentation in HIJING are converted to their valence quarks and antiquarks, whose evolution in time and space is guided by the ZPC model. After the end of their scatterings, quarks and antiquarks are converted to hadrons via a spatial coalescence model. In both versions of the AMPT model, the scatterings among hadrons are described by a relativistic transport (ART) model [48]. The (anti-)deuterons are pro-

duced and dissolved within ART via the $NN \leftrightarrow \pi d$ reaction in the hadronic stage of AMPT. The Monte Carlo predictions [49] for the deuteron coalescence parameter (B_2) and elliptic flow (v_2) are compared with the measured one in this section. For the simulation, an impact parameter $b = 8$ fm was used: this value corresponds to the mean value of the impact parameter in the 20–40% centrality interval [26]. The comparisons between data and Monte Carlo results can be seen in Fig. 9: in the left top panel the measured B_2 is shown (filled markers) together with the published AMPT expectations (lines), while in the bottom panel the ratios between

the data and models are shown. In the top right panel the measured elliptic flow (filled markers) and the AMPT expectations are displayed. From the bottom right panel of Fig. 9 it is possible to observe that the default version of AMPT (empty circles) is able to reproduce the measured deuteron elliptic flow, while the simulated B_2 is able to reproduce the behaviour of the measured one but is larger by a factor 2. The AMPT with String Melting enabled (dotted line in the top panels and full squares in the bottom panels) is unable to reproduce neither the measured B_2 nor the $v_2(p_T)$ parameter of the (anti-)deuterons. It is worth to emphasize that the standard AMPT does not reproduce the lighter hadrons $v_2(p_T)$ neither [35].

7 Conclusions

In this paper we presented the deuteron spectra up to $p_T = 8$ GeV/c produced in Pb–Pb collisions at $\sqrt{s_{NN}} = 2.76$ TeV extending significantly the p_T reached by the spectra shown in [2] for central and semi-central collisions. The v_2 of (anti-)deuterons is measured up to 5 GeV/c and it shows an increasing trend going from central to semi-central collisions, consistent with the picture of the final state anisotropy driven by the collision geometry. At low p_T the deuteron v_2 follows the mass ordering, indicating a more pronounced radial flow in the most central collisions, as it is observed also for lighter particles. Similarly the n_q scaling violation seen for the elliptic flow of lighter particles at the LHC energies is confirmed for the elliptic flow of the deuteron. The Blast-Wave model, fitted on the spectra and the elliptic flow of pions, kaons and protons, describes within the experimental uncertainties the deuteron production spectra for $p_T > 1.8$ GeV/c and the deuteron $v_2(p_T)$ suggesting common kinetic freeze-out conditions. At lower transverse momenta the model underestimates the measured spectra with a discrepancy up to 2σ . The coalescence parameter B_2 , evaluated up to $p_T/A = 4$ GeV/c, rapidly increases with the transverse momentum confirming the experimental observation made in [2]. The simplest formulation of the coalescence model [17] predicts a flat B_2 distribution and it does not reproduce the observed trend. The same model fails to reproduce the measured elliptic flow of deuterons. On the contrary, the AMPT model without String Melting [18] is able to reproduce the observed elliptic flow of deuterons and it correctly predicts the shape of the B_2 distribution but it overestimates the data by about a factor of 2. When enabling the String Melting mechanism the AMPT model is unable to predict neither the measured B_2 nor the $v_2(p_T)$ of the (anti-)deuterons.

Acknowledgements The ALICE Collaboration would like to thank all its engineers and technicians for their invaluable contributions to the construction of the experiment and the CERN accelerator teams for the

outstanding performance of the LHC complex. The ALICE Collaboration gratefully acknowledges the resources and support provided by all Grid centres and the Worldwide LHC Computing Grid (WLCG) collaboration. The ALICE Collaboration acknowledges the following funding agencies for their support in building and running the ALICE detector: A. I. Alikhanyan National Science Laboratory (Yerevan Physics Institute) Foundation (ANSL), State Committee of Science and World Federation of Scientists (WFS), Armenia; Austrian Academy of Sciences and Nationalstiftung für Forschung, Technologie und Entwicklung, Austria; Ministry of Communications and High Technologies, National Nuclear Research Center, Azerbaijan; Conselho Nacional de Desenvolvimento Científico e Tecnológico (CNPq), Universidade Federal do Rio Grande do Sul (UFRGS), Financiadora de Estudos e Projetos (Finep) and Fundação de Amparo à Pesquisa do Estado de São Paulo (FAPESP), Brazil; Ministry of Science and Technology of China (MSTC), National Natural Science Foundation of China (NSFC) and Ministry of Education of China (MOEC), China; Ministry of Science, Education and Sport and Croatian Science Foundation, Croatia; Ministry of Education, Youth and Sports of the Czech Republic, Czech Republic; The Danish Council for Independent Research/Natural Sciences, the Carlsberg Foundation and Danish National Research Foundation (DNRF), Denmark; Helsinki Institute of Physics (HIP), Finland; Commissariat à l’Energie Atomique (CEA) and Institut National de Physique Nucléaire et de Physique des Particules (IN2P3) and Centre National de la Recherche Scientifique (CNRS), France; Bundesministerium für Bildung, Wissenschaft, Forschung und Technologie (BMBF) and GSI Helmholtzzentrum für Schwerionenforschung GmbH, Germany; General Secretariat for Research and Technology, Ministry of Education, Research and Religions, Greece; National Research, Development and Innovation Office, Hungary; Department of Atomic Energy Government of India (DAE) and Council of Scientific and Industrial Research (CSIR), New Delhi, India; Indonesian Institute of Science, Indonesia; Centro Fermi-Museo Storico della Fisica e Centro Studi e Ricerche Enrico Fermi and Istituto Nazionale di Fisica Nucleare (INFN), Italy; Institute for Innovative Science and Technology, Nagasaki Institute of Applied Science (IIST), Japan Society for the Promotion of Science (JSPS) KAKENHI and Japanese Ministry of Education, Culture, Sports, Science and Technology (MEXT), Japan; Consejo Nacional de Ciencia (CONACYT) y Tecnología, through Fondo de Cooperación Internacional en Ciencia y Tecnología (FONCICYT) and Dirección General de Asuntos del Personal Académico (DGAPA), Mexico; Nederlandse Organisatie voor Wetenschappelijk Onderzoek (NWO), Netherlands; The Research Council of Norway, Norway; Commission on Science and Technology for Sustainable Development in the South (COMSATS), Pakistan; Pontificia Universidad Católica del Perú, Peru; Ministry of Science and Higher Education and National Science Centre, Poland; Korea Institute of Science and Technology Information and National Research Foundation of Korea (NRF), Republic of Korea; Ministry of Education and Scientific Research, Institute of Atomic Physics and Romanian National Agency for Science, Technology and Innovation, Romania; Joint Institute for Nuclear Research (JINR), Ministry of Education and Science of the Russian Federation and National Research Centre Kurchatov Institute, Russia; Ministry of Education, Science, Research and Sport of the Slovak Republic, Slovakia; National Research Foundation of South Africa, South Africa; Centro de Aplicaciones Tecnológicas y Desarrollo Nuclear (CEADEN), Cubaenergía, Cuba, Ministerio de Ciencia e Innovación and Centro de Investigaciones Energéticas, Medioambientales y Tecnológicas (CIEMAT), Spain; Swedish Research Council (VR) and Knut and Alice Wallenberg Foundation (KAW), Sweden; European Organization for Nuclear Research, Switzerland; National Science and Technology Development Agency (NSDTA), Suranaree University of Technology (SUT) and Office of the Higher Education Commission under NRU project of Thailand, Thailand; Turkish Atomic Energy Agency (TAEK), Turkey; National Academy of Sciences of Ukraine, Ukraine; Science and Technology Facilities Council (STFC), United Kingdom; National Science Foundation of the United States

of America (NSF) and United States Department of Energy, Office of Nuclear Physics (DOE NP), United States of America.

Open Access This article is distributed under the terms of the Creative Commons Attribution 4.0 International License (<http://creativecommons.org/licenses/by/4.0/>), which permits unrestricted use, distribution, and reproduction in any medium, provided you give appropriate credit to the original author(s) and the source, provide a link to the Creative Commons license, and indicate if changes were made. Funded by SCOAP³.

References

- ALICE Collaboration, K. Aamodt et al., The ALICE experiment at the CERN LHC. *JINST* **3**, S08002 (2008)
- ALICE Collaboration, J. Adam et al., Production of light nuclei and anti-nuclei in pp and Pb–Pb collisions at energies available at the CERN Large Hadron Collider. *Phys. Rev. C* **93**(2), 024917 (2016). [arXiv:1506.08951](https://arxiv.org/abs/1506.08951) [nucl-ex]
- NA49 Collaboration, T. Anticic et al., Production of deuterium, tritium, and He3 in central Pb + Pb collisions at 20A,30A,40A,80A, and 158A GeV at the CERN Super Proton Synchrotron. *Phys. Rev. C* **94**(4), 044906 (2016). [arXiv:1606.04234](https://arxiv.org/abs/1606.04234) [nucl-ex]
- PHENIX Collaboration, S.S. Adler et al., Deuteron and antideuteron production in Au + Au collisions at $\sqrt{s_{NN}} = 200$ GeV. *Phys. Rev. Lett.* **94**, 122302 (2005). [arXiv:nucl-ex/0406004](https://arxiv.org/abs/nucl-ex/0406004) [nucl-ex]
- STAR Collaboration, L. Adamczyk et al., Measurement of elliptic flow of light nuclei at $\sqrt{s_{NN}} = 200, 62.4, 39, 27, 19.6, 11.5,$ and 7.7 GeV at RHIC. [arXiv:1601.07052](https://arxiv.org/abs/1601.07052) [nucl-ex]
- J.-Y. Ollitrault, Anisotropy as a signature of transverse collective flow. *Phys. Rev. D* **46**, 229–245 (1992)
- S.A. Voloshin, A.M. Poskanzer, R. Snellings, Collective phenomena in non-central nuclear collisions. [arXiv:0809.2949](https://arxiv.org/abs/0809.2949) [nucl-ex]
- J.-Y. Ollitrault, A.M. Poskanzer, S.A. Voloshin, Effect of flow fluctuations and nonflow on elliptic flow methods. *Phys. Rev. C* **80**, 014904 (2009). [arXiv:0904.2315](https://arxiv.org/abs/0904.2315) [nucl-ex]
- B. Alver, G. Roland, Collision geometry fluctuations and triangular flow in heavy-ion collisions. *Phys. Rev. C* **81**, 054905 (2010). [arXiv:1003.0194](https://arxiv.org/abs/1003.0194) [nucl-th]. [Erratum: *Phys. Rev. C* **82**, 039903 (2010)]
- Z. Qiu, U.W. Heinz, Event-by-event shape and flow fluctuations of relativistic heavy-ion collision fireballs. *Phys. Rev. C* **84**, 024911 (2011). [arXiv:1104.0650](https://arxiv.org/abs/1104.0650) [nucl-th]
- S. Voloshin, Y. Zhang, Flow study in relativistic nuclear collisions by Fourier expansion of Azimuthal particle distributions. *Z. Phys. C* **70**, 665–672 (1996). [arXiv:hep-ph/9407282](https://arxiv.org/abs/hep-ph/9407282) [hep-ph]
- C. Nonaka, B. Muller, M. Asakawa, S.A. Bass, R.J. Fries, Elliptic flow of resonances at RHIC: probing final state interactions and the structure of resonances. *Phys. Rev. C* **69**, 031902 (2004). [arXiv:nucl-th/0312081](https://arxiv.org/abs/nucl-th/0312081) [nucl-th]
- G.D. Westfall, J. Gosset, P.J. Johansen, A.M. Poskanzer, W.G. Meyer, H.H. Gutbrod, A. Sandoval, R. Stock, Nuclear fireball model for proton inclusive spectra from relativistic heavy ion collisions. *Phys. Rev. Lett.* **37**, 1202–1205 (1976)
- E. Schnedermann, J. Sollfrank, U.W. Heinz, Thermal phenomenology of hadrons from 200-A/GeV S+S collisions. *Phys. Rev. C* **48**, 2462–2475 (1993). [arXiv:nucl-th/9307020](https://arxiv.org/abs/nucl-th/9307020) [nucl-th]
- P. Huovinen, P.F. Kolb, U.W. Heinz, P.V. Ruuskanen, S.A. Voloshin, Radial and elliptic flow at RHIC: further predictions. *Phys. Lett. B* **503**, 58–64 (2001). [arXiv:hep-ph/0101136](https://arxiv.org/abs/hep-ph/0101136) [hep-ph]
- STAR Collaboration, C. Adler et al., Identified particle elliptic flow in Au + Au collisions at $\sqrt{s_{NN}} = 130$ GeV. *Phys. Rev. Lett.* **87**, 182301 (2001). [arXiv:nucl-ex/0107003](https://arxiv.org/abs/nucl-ex/0107003) [nucl-ex]
- L. Csernai, J.I. Kapusta, Entropy and cluster production in nuclear collisions. *Phys. Rep.* **131**, 223–318 (1986)
- Z.-W. Lin, C.M. Ko, B.-A. Li, B. Zhang, S. Pal, A multi-phase transport model for relativistic heavy ion collisions. *Phys. Rev. C* **72**, 064901 (2005). [arXiv:nucl-th/0411110](https://arxiv.org/abs/nucl-th/0411110) [nucl-th]
- ALICE Collaboration, B. Abelev et al., Performance of the ALICE experiment at the CERN LHC. *Int. J. Mod. Phys. A* **29**, 1430044 (2014). [arXiv:1402.4476](https://arxiv.org/abs/1402.4476) [nucl-ex]
- ALICE Collaboration, E. Abbas et al., Performance of the ALICE VZERO system. *JINST* **8**, P10016 (2013). [arXiv:1306.3130](https://arxiv.org/abs/1306.3130) [nucl-ex]
- ALICE Collaboration, K. Aamodt et al., Alignment of the ALICE inner tracking system with cosmic-ray tracks. *JINST* **5**, P03003 (2010). [arXiv:1001.0502](https://arxiv.org/abs/1001.0502) [physics.ins-det]
- J. Alme, Y. Andres, H. Appelshäuser, S. Bablok, N. Bialas et al., The ALICE TPC, a large 3-dimensional tracking device with fast readout for ultra-high multiplicity events. *Nucl. Instrum. Methods A* **622**, 316–367 (2010). [arXiv:1001.1950](https://arxiv.org/abs/1001.1950) [physics.ins-det]
- A. Akimov et al., Performance of the ALICE Time-Of-Flight detector at the LHC. *Eur. Phys. J. Plus* **128**, 44 (2013)
- ALICE Collaboration, J. Adam et al., Centrality dependence of the nuclear modification factor of charged pions, kaons, and protons in Pb–Pb collisions at $\sqrt{s_{NN}} = 2.76$ TeV. *Phys. Rev. C* **93**(3), 034913 (2016). [arXiv:1506.07287](https://arxiv.org/abs/1506.07287) [nucl-ex]
- ALICE Collaboration, K. Aamodt et al., Centrality dependence of the charged-particle multiplicity density at mid-rapidity in Pb–Pb collisions at $\sqrt{s_{NN}} = 2.76$ TeV. *Phys. Rev. Lett.* **106**, 032301 (2011). [arXiv:1012.1657](https://arxiv.org/abs/1012.1657) [nucl-ex]
- ALICE Collaboration, B. Abelev et al., Centrality determination of Pb–Pb collisions at $\sqrt{s_{NN}} = 2.76$ TeV with ALICE. *Phys. Rev. C* **88**, 044909 (2013). [arXiv:1301.4361](https://arxiv.org/abs/1301.4361) [nucl-ex]
- ALICE Collaboration, J. Adam et al., ${}^3_{\Lambda}$ H and ${}^3_{\Lambda}\bar{H}$ production in Pb–Pb collisions at $\sqrt{s_{NN}} = 2.76$ TeV. *Phys. Lett. B* **754**, 360–372 (2016). [arXiv:1506.08453](https://arxiv.org/abs/1506.08453) [nucl-ex]
- Particle Data Group Collaboration, C. Patrignani et al., Review of particle physics. *Chin. Phys. C* **40**(10), 100001 (2016)
- X.-N. Wang, M. Gyulassy, HIJING: a Monte Carlo model for multiple jet production in p p, p A and A A collisions. *Phys. Rev. D* **44**, 3501–3516 (1991)
- R. Brun, F. Carminati, S. Giani, GEANT detector description and simulation tool. Program Library Long Write-up W5013 (1994)
- A. Moiseev, J. Ormes, Inelastic cross section for antihelium on nuclei: an empirical formula for use in the experiments to search for cosmic antimatter. *Astropart. Phys.* **6**(3), 379–386 (1997). <http://www.sciencedirect.com/science/article/pii/S0927650596000710>
- Geant4 Collaboration, S. Agostinelli et al., Geant4: a simulation toolkit. *Nucl. Instrum. Methods A* **506**, 250–303 (2003)
- Geant4 Hadronics Working Group Collaboration, A. Galoyan, V. Uzhinsky, Simulations of light antinucleus–nucleus interactions. *Hyperfine Interact* **215**(1–3), 69–76 (2013). [arXiv:1208.3614](https://arxiv.org/abs/1208.3614) [nucl-th]
- E. Schnedermann, J. Sollfrank, U.W. Heinz, Thermal phenomenology of hadrons from 200A GeV S+S collisions. *Phys. Rev.* **48**, 2462–2475 (1993). [arXiv:nucl-th/9307020](https://arxiv.org/abs/nucl-th/9307020) [nucl-th]
- ALICE Collaboration, B.B. Abelev et al., Elliptic flow of identified hadrons in Pb–Pb collisions at $\sqrt{s_{NN}} = 2.76$ TeV. *JHEP* **06**, 190 (2015). [arXiv:1405.4632](https://arxiv.org/abs/1405.4632) [nucl-ex]
- A.M. Poskanzer, S.A. Voloshin, Methods for analyzing anisotropic flow in relativistic nuclear collisions. *Phys. Rev. C* **58**, 1671–1678 (1998)
- C. Shen, U. Heinz, P. Huovinen, H. Song, Radial and elliptic flow in Pb+Pb collisions at the Large Hadron Collider from viscous hydrodynamic. *Phys. Rev. C* **84**, 044903 (2011). [arXiv:1105.3226](https://arxiv.org/abs/1105.3226) [nucl-th]

38. STAR Collaboration, J. Adams et al., Particle type dependence of azimuthal anisotropy and nuclear modification of particle production in Au + Au collisions at $\sqrt{s_{NN}} = 200$ GeV. Phys. Rev. Lett. **92**, 052302 (2004). [arXiv:nucl-ex/0306007](#) [nucl-ex]
39. STAR Collaboration, B.I. Abelev et al., Mass, quark-number, and $\sqrt{s_{NN}}$ dependence of the second and fourth flow harmonics in ultra-relativistic nucleus–nucleus collisions. Phys. Rev. C **75**, 054906 (2007). [arXiv:nucl-ex/0701010](#) [nucl-ex]
40. PHENIX Collaboration, A. Adare et al., Scaling properties of azimuthal anisotropy in Au+Au and Cu+Cu collisions at $\sqrt{s_{NN}} = 200$ GeV. Phys. Rev. Lett. **98**, 162301 (2007). [arXiv:nucl-ex/0608033](#) [nucl-ex]
41. PHENIX Collaboration, S. Afanasiev et al., Elliptic flow for phi mesons and (anti)deuterons in Au + Au collisions at $\sqrt{s_{NN}} = 200$ GeV. Phys. Rev. Lett. **99**, 052301 (2007). [arXiv:nucl-ex/0703024](#) [NUCL-EX]
42. PHENIX Collaboration, S.S. Adler et al., Elliptic flow of identified hadrons in Au+Au collisions at $\sqrt{s_{NN}} = 200$ GeV. Phys. Rev. Lett. **91**, 182301 (2003). [arXiv:nucl-ex/0305013](#) [nucl-ex]
43. PHENIX Collaboration, A. Adare et al., Deviation from quark-number scaling of the anisotropy parameter v_2 of pions, kaons, and protons in Au+Au collisions at $\sqrt{s_{NN}} = 200$ GeV. Phys. Rev. C **85**, 064914 (2012). [arXiv:1203.2644](#) [nucl-ex]
44. ALICE Collaboration, B. Abelev et al., Centrality dependence of π , K, p production in Pb–Pb collisions at $\sqrt{s_{NN}} = 2.76$ TeV. Phys. Rev. C **88**, 044910 (2013). [arXiv:1303.0737](#) [hep-ex]
45. A. Polleri, J.P. Bondorf, I.N. Mishustin, Effects of collective expansion on light cluster spectra in relativistic heavy ion collisions. Phys. Lett. B **419**, 19–24 (1998). [arXiv:nucl-th/9711011](#) [nucl-th]
46. D. Molnar, S.A. Voloshin, Elliptic flow at large transverse momenta from quark coalescence. Phys. Rev. Lett. **91**, 092301 (2003). [arXiv:nucl-th/0302014](#) [nucl-th]
47. B. Zhang, ZPC 1.0.1: a parton cascade for ultrarelativistic heavy ion collisions. Comput. Phys. Commun. **109**, 193–206 (1998). [arXiv:nucl-th/9709009](#) [nucl-th]
48. B.-A. Li, C.M. Ko, Formation of superdense hadronic matter in high-energy heavy ion collisions. Phys. Rev. C **52**, 2037–2063 (1995). [arXiv:nucl-th/9505016](#) [nucl-th]
49. L. Zhu, C.M. Ko, X. Yin, Light (anti)-nuclei production and flow in relativistic heavy-ion collisions. Phys. Rev. C **92**, 064911 (2015). [arXiv:1510.03568](#) [nucl-th]

ALICE Collaboration

S. Acharya¹³⁹, D. Adamová⁹⁶, J. Adolfsson³⁴, M. M. Aggarwal¹⁰¹, G. Aglieri Rinella³⁵, M. Agnello³¹, N. Agrawal⁴⁸, Z. Ahammed¹³⁹, N. Ahmad¹⁷, S. U. Ahn⁸⁰, S. Aiola¹⁴³, A. Akindinov⁶⁵, S. N. Alam¹³⁹, J. L. B. Alba¹¹⁴, D. S. D. Albuquerque¹²⁵, D. Aleksandrov⁹², B. Alessandro⁵⁹, R. Alfaro Molina⁷⁵, A. Alici^{12,27,54}, A. Alkin³, J. Alme²², T. Alt⁷¹, L. Altenkamper²², I. Altsybeev¹³⁸, C. Alves Garcia Prado¹²⁴, C. Andrei⁸⁹, D. Andreou³⁵, H. A. Andrews¹¹³, A. Andronic¹⁰⁹, V. Anguelov¹⁰⁶, C. Anson⁹⁹, T. Antičić¹¹⁰, F. Antinori⁵⁷, P. Antonioli⁵⁴, R. Anwar¹²⁷, L. Aphecetche¹¹⁷, H. Appelshäuser⁷¹, S. Arcelli²⁷, R. Arnaldi⁵⁹, O. W. Arnold^{36,107}, I. C. Arsene²¹, M. Arslandok¹⁰⁶, B. Audurier¹¹⁷, A. Augustinus³⁵, R. Averbeck¹⁰⁹, M. D. Azmi¹⁷, A. Badalá⁵⁶, Y. W. Baek^{61,79}, S. Bagnasco⁵⁹, R. Bailhache⁷¹, R. Bala¹⁰³, A. Baldisseri⁷⁶, M. Ball⁴⁵, R. C. Baral⁶⁸, A. M. Barbano²⁶, R. Barbera²⁸, F. Barile^{33,53}, L. Barioglio²⁶, G. G. Barnaföldi¹⁴², L. S. Barnby⁹⁵, V. Barret⁸², P. Bartalini⁷, K. Barth³⁵, E. Bartsch⁷¹, M. Basile²⁷, N. Bastid⁸², S. Basu¹⁴¹, B. Bathen⁷², G. Batigne¹¹⁷, B. Batyunya⁷⁸, P. C. Batzing²¹, I. G. Bearden⁹³, H. Beck¹⁰⁶, C. Bedda⁶⁴, N. K. Behera⁶¹, I. Belikov¹³⁵, F. Bellini²⁷, H. Bello Martinez², R. Bellwied¹²⁷, L. G. E. Beltran¹²³, V. Belyaev⁸⁵, G. Bencedi¹⁴², S. Beole²⁶, A. Bercuci⁸⁹, Y. Berdnikov⁹⁸, D. Berenyi¹⁴², R. A. Bertens¹³⁰, D. Berzano³⁵, L. Betev³⁵, A. Bhasin¹⁰³, I. R. Bhat¹⁰³, A. K. Bhati¹⁰¹, B. Bhattacharjee⁴⁴, J. Bhom¹²¹, L. Bianchi¹²⁷, N. Bianchi⁵¹, C. Bianchin¹⁴¹, J. Bielčík³⁹, J. Bielčíková⁹⁶, A. Bilandzic^{36,107}, G. Biro¹⁴², R. Biswas⁴, S. Biswas⁴, J. T. Blair¹²², D. Blau⁹², C. Blume⁷¹, G. Boca¹³⁶, F. Bock^{35,84,106}, A. Bogdanov⁸⁵, L. Boldizsár¹⁴², M. Bombara⁴⁰, G. Bonomi¹³⁷, M. Bonora³⁵, J. Book⁷¹, H. Borel⁷⁶, A. Borissov¹⁹, M. Borri¹²⁹, E. Botta²⁶, C. Bourjau⁹³, L. Bratrud⁷¹, P. Braun-Munzinger¹⁰⁹, M. Bregant¹²⁴, T. A. Broker⁷¹, M. Broz³⁹, E. J. Brucken⁴⁶, E. Bruna⁵⁹, G. E. Bruno³³, D. Budnikov¹¹¹, H. Buesching⁷¹, S. Bufalino³¹, P. Buhler¹¹⁶, P. Buncic³⁵, O. Busch¹³³, Z. Buthelezi⁷⁷, J. B. Butt¹⁵, J. T. Buxton¹⁸, J. Cabala¹¹⁹, D. Caffarri^{35,94}, H. Caines¹⁴³, A. Caliva⁶⁴, E. Calvo Villar¹¹⁴, P. Camerini²⁵, A. A. Capon¹¹⁶, F. Carena³⁵, W. Carena³⁵, F. Carnesecchi^{12,27}, J. Castillo Castellanos⁷⁶, A. J. Castro¹³⁰, E. A. R. Casula⁵⁵, C. Ceballos Sanchez⁹, P. Cerello⁵⁹, S. Chandra¹³⁹, B. Chang¹²⁸, S. Chapeland³⁵, M. Chartier¹²⁹, J. L. Charvet⁷⁶, S. Chattopadhyay¹³⁹, S. Chattopadhyay¹¹², A. Chauvin^{36,107}, M. Cherney⁹⁹, C. Cheshkov¹³⁴, B. Cheynis¹³⁴, V. Chibante Barroso³⁵, D. D. Chinellato¹²⁵, S. Cho⁶¹, P. Chochula³⁵, K. Choi¹⁹, M. Chojnacki⁹³, S. Choudhury¹³⁹, T. Chowdhury⁸², P. Christakoglou⁹⁴, C. H. Christensen⁹³, P. Christiansen³⁴, T. Chujo¹³³, S. U. Chung¹⁹, C. Cicalo⁵⁵, L. Cifarelli^{12,27}, F. Cindolo⁵⁴, J. Cleymans¹⁰², F. Colamaria³³, D. Colella^{35,66}, A. Collu⁸⁴, M. Colocci²⁷, M. Concas^{59,b}, G. Conesa Balbastre⁸³, Z. Conesa del Valle⁶², M. E. Connors^{143,c}, J. G. Contreras³⁹, T. M. Cormier⁹⁷, Y. Corrales Morales⁵⁹, I. Cortés Maldonado², P. Cortese³², M. R. Cosentino¹²⁶, F. Costa³⁵, S. Costanza¹³⁶, J. Crković⁶², P. Crochet⁸², E. Cuautele⁷³, L. Cunqueiro⁷², T. Dahms^{36,107}, A. Dainese⁵⁷, M. C. Danisch¹⁰⁶, A. Danu⁶⁹, D. Das¹¹², I. Das¹¹², S. Das⁴, A. Dash⁹⁰, S. Dash⁴⁸, S. De^{49,124}, A. De Caro³⁰, G. de Cataldo⁵³, C. de Conti¹²⁴, J. de Cuveland⁴², A. De Falco²⁴, D. De Gruttola^{12,30}, N. De Marco⁵⁹, S. De Pasquale³⁰, R. D. De Souza¹²⁵, H. F. Degenhardt¹²⁴, A. Deisting^{106,109}, A. Deloff⁸⁸, C. Deplano⁹⁴, P. Dhankher⁴⁸, D. Di Bari³³, A. Di Mauro³⁵, P. Di Nezza⁵¹, B. Di Ruzza⁵⁷, M. A. Diaz Corchero¹⁰, T. Dietel¹⁰², P. Dillenseger⁷¹, R. Divià³⁵, Ø. Djuvsland²², A. Dobrin³⁵, D. Domenicis Gimenez¹²⁴, B. Dönigus⁷¹, O. Dordic²¹, L. V. V. Doremalen⁶⁴, A. K. Dubey¹³⁹

A. Dubla¹⁰⁹, L. Ducroux¹³⁴, A. K. Duggal¹⁰¹, P. Dupieux⁸², R. J. Ehlers¹⁴³, D. Elia⁵³, E. Endress¹¹⁴, H. Engel⁷⁰, E. Eppe¹⁴³, B. Erazmus¹¹⁷, F. Erhardt¹⁰⁰, B. Espagnon⁶², S. Esumi¹³³, G. Eulisse³⁵, J. Eum¹⁹, D. Evans¹¹³, S. Evdokimov¹¹⁵, L. Fabbietti^{36,107}, J. Faivre⁸³, A. Fantoni⁵¹, M. Fasel^{84,97}, L. Feldkamp⁷², A. Feliciello⁵⁹, G. Feofilov¹³⁸, J. Ferencei⁹⁶, A. Fernández Téllez², E. G. Ferreira¹⁶, A. Ferretti²⁶, A. Festanti^{29,35}, V. J. G. Feuillard^{76,82}, J. Figiel¹²¹, M. A. S. Figueredo¹²⁴, S. Filchagin¹¹¹, D. Finogeev⁶³, F. M. Fionda^{22,24}, E. M. Fiore³³, M. Floris³⁵, S. Foertsch⁷⁷, P. Foka¹⁰⁹, S. Fokin⁹², E. Fragiaco⁶⁰, A. Francescon³⁵, A. Francisco¹¹⁷, U. Frankenfeld¹⁰⁹, G. G. Fronze²⁶, U. Fuchs³⁵, C. Furget⁸³, A. Furs⁶³, M. Fusco Girard³⁰, J. J. Gaardhøje⁹³, M. Gagliardi²⁶, A. M. Gago¹¹⁴, K. Gajdosova⁹³, M. Gallio²⁶, C. D. Galvan¹²³, P. Ganoti⁸⁷, C. Gao⁷, C. Garabatos¹⁰⁹, E. Garcia-Solis¹³, K. Garg²⁸, C. Gargiulo³⁵, P. Gasik^{36,107}, E. F. Gauger¹²², M. B. Gay Ducati⁷⁴, M. Germain¹¹⁷, J. Ghosh¹¹², P. Ghosh¹³⁹, S. K. Ghosh⁴, P. Gianotti⁵¹, P. Giubellino^{35,59,109}, P. Giubilato²⁹, E. Gladysz-Dziadus¹²¹, P. Glässel¹⁰⁶, D. M. Gómez Coral⁷⁵, A. Gomez Ramirez⁷⁰, A. S. Gonzalez³⁵, V. Gonzalez¹⁰, P. González-Zamora¹⁰, S. Gorbunov⁴², L. Görlich¹²¹, S. Gotovac¹²⁰, V. Grabski⁷⁵, L. K. Graczykowski¹⁴⁰, K. L. Graham¹¹³, L. Greiner⁸⁴, A. Grelli⁶⁴, C. Grigoras³⁵, V. Grigoriev⁸⁵, A. Grigoryan¹, S. Grigoryan⁷⁸, N. Grion⁶⁰, J. M. Gronefeld¹⁰⁹, F. Grosa³¹, J. F. Grosse-Oetringhaus³⁵, R. Grosso¹⁰⁹, L. Gruber¹¹⁶, F. Guber⁶³, R. Guernane⁸³, B. Guerzoni²⁷, K. Gulbrandsen⁹³, T. Gunji¹³², A. Gupta¹⁰³, R. Gupta¹⁰³, I. B. Guzman², R. Haake³⁵, C. Hadjidakis⁶², H. Hamagaki^{86,132}, G. Hamar¹⁴², J. C. Hamon¹³⁵, M. R. Haque⁶⁴, J. W. Harris¹⁴³, A. Harton¹³, H. Hassan⁸³, D. Hatzifotiadou^{12,54}, S. Hayashi¹³², S. T. Heckel⁷¹, E. Hellbär⁷¹, H. Helstrup³⁷, A. Herghelegiu⁸⁹, G. Herrera Corral¹¹, F. Herrmann⁷², B. A. Hess¹⁰⁵, K. F. Hetland³⁷, H. Hillemanns³⁵, C. Hills¹²⁹, B. Hippolyte¹³⁵, J. Hladky⁶⁷, B. Hohlweger¹⁰⁷, D. Horak³⁹, S. Hornung¹⁰⁹, R. Hosokawa^{83,133}, P. Hristov³⁵, C. Hughes¹³⁰, T. J. Humanic¹⁸, N. Hussain⁴⁴, T. Hussain¹⁷, D. Hutter⁴², D. S. Hwang²⁰, S. A. Iga Buitron⁷³, R. Ilkaev¹¹¹, M. Inaba¹³³, M. Ippolitov^{85,92}, M. Irfan¹⁷, V. Isakov⁶³, M. Ivanov¹⁰⁹, V. Ivanov⁹⁸, V. Izucheev¹¹⁵, B. Jacak⁸⁴, N. Jacazio²⁷, P. M. Jacobs⁸⁴, M. B. Jadhav⁴⁸, J. Jadlovsky¹¹⁹, S. Jaelani⁶⁴, C. Jahnke³⁶, M. J. Jakubowska¹⁴⁰, M. A. Janik¹⁴⁰, P. H. S. Y. Jayarathna¹²⁷, C. Jena⁹⁰, S. Jena¹²⁷, M. Jercic¹⁰⁰, R. T. Jimenez Bustamante¹⁰⁹, P. G. Jones¹¹³, A. Jusko¹¹³, P. Kalinak⁶⁶, A. Kalweit³⁵, J. H. Kang¹⁴⁴, V. Kaplin⁸⁵, S. Kar¹³⁹, A. Karasu Uysal⁸¹, O. Karavichev⁶³, T. Karavicheva⁶³, L. Karayan^{106,109}, P. Karczmarczyk³⁵, E. Karpechev⁶³, U. Keschull⁷⁰, R. Keidel¹⁴⁵, D. L. D. Keijdener⁶⁴, M. Keil³⁵, B. Ketzer⁴⁵, Z. Khabanova⁹⁴, P. Khan¹¹², S. A. Khan¹³⁹, A. Khanzadeev⁹⁸, Y. Kharlov¹¹⁵, A. Khatun¹⁷, A. Khuntia⁴⁹, M. M. Kielbowicz¹²¹, B. Kileng³⁷, B. Kim¹³³, D. Kim¹⁴⁴, D. W. Kim⁴³, D. J. Kim¹²⁸, H. Kim¹⁴⁴, J. S. Kim⁴³, J. Kim¹⁰⁶, M. Kim⁶¹, M. Kim¹⁴⁴, S. Kim²⁰, T. Kim¹⁴⁴, S. Kirsch⁴², I. Kisel⁴², S. Kiselev⁶⁵, A. Kisiel¹⁴⁰, G. Kiss¹⁴², J. L. Klay⁶, C. Klein⁷¹, J. Klein³⁵, C. Klein-Bösing⁷², S. Klewin¹⁰⁶, A. Kluge³⁵, M. L. Knichel¹⁰⁶, A. G. Knospe¹²⁷, C. Kobdaj¹¹⁸, M. Kofarago¹⁴², T. Kollegger¹⁰⁹, A. Kolojvari¹³⁸, V. Kondratiev¹³⁸, N. Kondratyeva⁸⁵, E. Kondratyuk¹¹⁵, A. Konevskikh⁶³, M. Konyushikhin¹⁴¹, M. Kopicik¹¹⁹, M. Kour¹⁰³, C. Kouzinopoulos³⁵, O. Kovalenko⁸⁸, V. Kovalenko¹³⁸, M. Kowalski¹²¹, G. Koyithatta Meethalevedu⁴⁸, I. Králik⁶⁶, A. Kravčáková⁴⁰, M. Krivda^{66,113}, F. Krizek⁹⁶, E. Kryshen⁹⁸, M. Krzewicki⁴², A. M. Kubera¹⁸, V. Kučera⁹⁶, C. Kuhn¹³⁵, P. G. Kuijper⁹⁴, A. Kumar¹⁰³, J. Kumar⁴⁸, L. Kumar¹⁰¹, S. Kumar⁴⁸, S. Kundu⁹⁰, P. Kurashvili⁸⁸, A. Kurepin⁶³, A. B. Kurepin⁶³, A. Kuryakin¹¹¹, S. Kuschpil⁹⁶, M. J. Kweon⁶¹, Y. Kwon¹⁴⁴, S. L. La Pointe⁴², P. La Rocca²⁸, C. Lagana Fernandes¹²⁴, Y. S. Lai⁸⁴, I. Lakomov³⁵, R. Langoy⁴¹, K. Lapidus¹⁴³, C. Lara⁷⁰, A. Lardeux^{21,76}, A. Lattuca²⁶, E. Laudi³⁵, R. Lavicka³⁹, L. Lazaridis³⁵, R. Lea²⁵, L. Leardini¹⁰⁶, S. Lee¹⁴⁴, F. Lehas⁹⁴, S. Lehner¹¹⁶, J. Lehrbach⁴², R. C. Lemmon⁹⁵, V. Lenti⁵³, E. Leogrande⁶⁴, I. León Monzón¹²³, P. Lévai¹⁴², S. Li⁷, X. Li¹⁴, J. Lien⁴¹, R. Lietava¹¹³, B. Lim¹⁹, S. Lindal²¹, V. Lindenstruth⁴², S. W. Lindsay¹²⁹, C. Lippmann¹⁰⁹, M. A. Lisa¹⁸, V. Litichevskiy⁴⁶, H. M. Ljunggren³⁴, W. J. Llope¹⁴¹, D. F. Lodato⁶⁴, P. I. Loenne²², V. Loginov⁸⁵, C. Loizides⁸⁴, P. Loncar¹²⁰, X. Lopez⁸², E. López Torres⁹, A. Lowe¹⁴², P. Luetig⁷¹, M. Lunardon²⁹, G. Luparello^{25,60}, M. Lupi³⁵, T. H. Lutz¹⁴³, A. Maevskaya⁶³, M. Mager³⁵, S. Mahajan¹⁰³, S. M. Mahmood²¹, A. Maire¹³⁵, R. D. Majka¹⁴³, M. Malaev⁹⁸, L. Malinina^{78,d}, D. Mal'kevich⁶⁵, P. Malzacher¹⁰⁹, A. Mamonov¹¹¹, V. Manko⁹², F. Manso⁸², V. Manzari⁵³, Y. Mao⁷, M. Marchisone^{77,131}, J. Mareš⁶⁷, G. V. Margagliotti²⁵, A. Margotti⁵⁴, J. Margutti⁶⁴, A. Marín¹⁰⁹, C. Markert¹²², M. Marquard⁷¹, N. A. Martin¹⁰⁹, P. Martinengo³⁵, J. A. L. Martinez⁷⁰, M. I. Martínez², G. Martínez García¹¹⁷, M. Martinez Pedreira³⁵, A. Mas¹²⁴, S. Masciocchi¹⁰⁹, M. Maserà²⁶, A. Masoni⁵⁵, E. Masson¹¹⁷, A. Mastroserio⁵³, A. M. Mathis^{36,107}, A. Matyjka^{121,130}, C. Mayer¹²¹, J. Mazer¹³⁰, M. Mazzilli³³, M. A. Mazzoni⁵⁸, F. Meddi²³, Y. Melikyan⁸⁵, A. Menchaca-Rocha⁷⁵, E. Meninno³⁰, J. Mercado Pérez¹⁰⁶, M. Meres³⁸, S. Mhlanga¹⁰², Y. Miake¹³³, M. M. Mieskolainen⁴⁶, D. Mihaylov¹⁰⁷, D. L. Mihaylov¹⁰⁷, K. Mikhaylov^{65,78}, L. Milano⁸⁴, J. Milosevic²¹, A. Mischke⁶⁴, A. N. Mishra⁴⁹, D. Miśkowiec¹⁰⁹, J. Mitra¹³⁹, C. M. Mitu⁶⁹, N. Mohammadi⁶⁴, B. Mohanty⁹⁰, M. Mohisin Khan^{17,e}, E. Montes¹⁰, D. A. Moreira De Godoy⁷², L. A. P. Moreno², S. Moretto²⁹, A. Morreale¹¹⁷, A. Morsch³⁵, V. Muccifora⁵¹, E. Mudnic¹²⁰, D. Mühlheim⁷², S. Muhuri¹³⁹, M. Mukherjee⁴, J. D. Mulligan¹⁴³, M. G. Munhoz¹²⁴, K. Munning⁴⁵, R. H. Munzer⁷¹, H. Murakami¹³², S. Murray⁷⁷, L. Musa³⁵, J. Musinsky⁶⁶, C. J. Myers¹²⁷, J. W. Myrcha¹⁴⁰, B. Naik⁴⁸, R. Nair⁸⁸, B. K. Nandi⁴⁸, R. Nania^{12,54}, E. Nappi⁵³, A. Narayan⁴⁸, M. U. Naru¹⁵, H. Natal da Luz¹²⁴, C. Nattrass¹³⁰, S. R. Navarro², K. Nayak⁹⁰, R. Nayak⁴⁸, T. K. Nayak¹³⁹, S. Nazarenko¹¹¹, A. Nedosekin⁶⁵, R. A. Negrao De Oliveira³⁵

L. Nellen⁷³, S. V. Nesbo³⁷, F. Ng¹²⁷, M. Nicassio¹⁰⁹, M. Niculescu⁶⁹, J. Niedziela^{35,140}, B. S. Nielsen⁹³, S. Nikolaev⁹², S. Nikulin⁹², V. Nikulin⁹⁸, A. Nobuhiro⁴⁷, F. Noferini^{12,54}, P. Nomokonov⁷⁸, G. Nooren⁶⁴, J. C. C. Noris², J. Norman¹²⁹, A. Nyanin⁹², J. Nystrand²², H. Oeschler^{106,a}, S. Oh¹⁴³, A. Ohlson^{35,106}, T. Okubo⁴⁷, L. Olah¹⁴², J. Oleniacz¹⁴⁰, A. C. Oliveira Da Silva¹²⁴, M. H. Oliver¹⁴³, J. Onderwaater¹⁰⁹, C. Oppedisano⁵⁹, R. Orava⁴⁶, M. Oravec¹¹⁹, A. Ortiz Velasquez⁷³, A. Oskarsson³⁴, J. Otwinowski¹²¹, K. Oyama⁸⁶, Y. Pachmayer¹⁰⁶, V. Pacik⁹³, D. Pagano¹³⁷, P. Pagano³⁰, G. Paic⁷³, P. Palni⁷, J. Pan¹⁴¹, A. K. Pandey⁴⁸, S. Panebianco⁷⁶, V. Papikyan¹, G. S. Pappalardo⁵⁶, P. Pareek⁴⁹, J. Park⁶¹, S. Parmar¹⁰¹, A. Passfeld⁷², S. P. Pathak¹²⁷, V. Paticchio⁵³, R. N. Patra¹³⁹, B. Paul⁵⁹, H. Pei⁷, T. Peitzmann⁶⁴, X. Peng⁷, L. G. Pereira⁷⁴, H. Pereira Da Costa⁷⁶, D. Peresunko^{85,92}, E. Perez Lezama⁷¹, V. Peskov⁷¹, Y. Pestov⁵, V. Petráček³⁹, V. Petrov¹¹⁵, M. Petrovici⁸⁹, C. Petta²⁸, R. P. Pezzi⁷⁴, S. Piano⁶⁰, M. Pikna³⁸, P. Pillot¹¹⁷, L. O. D. L. Pimentel⁹³, O. Pinazza^{35,54}, L. Pinsky¹²⁷, D. B. Piyarathna¹²⁷, M. Płoskoń⁸⁴, M. Planinic¹⁰⁰, F. Pliquett⁷¹, J. Pluta¹⁴⁰, S. Pochybova¹⁴², P. L. M. Podesta-Lerma¹²³, M. G. Poghosyan⁹⁷, B. Polichtchouk¹¹⁵, N. Poljak¹⁰⁰, W. Poonsawat¹¹⁸, A. Pop⁸⁹, H. Poppenborg⁷², S. Porteboeuf-Houssais⁸², J. Porter⁸⁴, V. Pozdniakov⁷⁸, S. K. Prasad⁴, R. Preghenella⁵⁴, F. Prino⁵⁹, C. A. Pruneau¹⁴¹, I. Pshenichnov⁶³, M. Puccio²⁶, G. Puddu²⁴, P. Pujahari¹⁴¹, V. Punin¹¹¹, J. Putschke¹⁴¹, A. Rachevski⁶⁰, S. Raha⁴, S. Rajput¹⁰³, J. Rak¹²⁸, A. Rakotozafindrabe⁷⁶, L. Ramello³², F. Rami¹³⁵, D. B. Rana¹²⁷, R. Raniwala¹⁰⁴, S. Raniwala¹⁰⁴, S. S. Räsänen⁴⁶, B. T. Rascanu⁷¹, D. Rathee¹⁰¹, V. Ratza⁴⁵, I. Ravasenga³¹, K. F. Read^{97,130}, K. Redlich^{88,f}, A. Rehman²², P. Reichelt⁷¹, F. Reidt³⁵, X. Ren⁷, R. Renfordt⁷¹, A. R. Reolon⁵¹, A. Reshetin⁶³, K. Reygers¹⁰⁶, V. Riabov⁹⁸, R. A. Ricci⁵², T. Richert⁶⁴, M. Richter²¹, P. Riedler³⁵, W. Riegler³⁵, F. Riggi²⁸, C. Ristea⁶⁹, M. Rodríguez Cahuantzi², K. Røed²¹, E. Rogochaya⁷⁸, D. Rohr^{35,42}, D. Röhrich²², P. S. Rokita¹⁴⁰, F. Ronchetti⁵¹, E. D. Rosas⁷³, P. Rosnet⁸², A. Rossi^{29,57}, A. Rotondi¹³⁶, F. Roukoutakis⁸⁷, A. Roy⁴⁹, C. Roy¹³⁵, P. Roy¹¹², A. J. Rubio Montero¹⁰, O. V. Rueda⁷³, R. Rui²⁵, B. Rumyantsev⁷⁸, A. Rustamov⁹¹, E. Ryabinkin⁹², Y. Ryabov⁹⁸, A. Rybicki¹²¹, S. Saarinen⁴⁶, S. Sadhu¹³⁹, S. Sadovsky¹¹⁵, K. Šafařík³⁵, S. K. Saha¹³⁹, B. Sahlmuller⁷¹, B. Sahoo⁴⁸, P. Sahoo⁴⁹, R. Sahoo⁴⁹, S. Sahoo⁶⁸, P. K. Sahu⁶⁸, J. Saini¹³⁹, S. Sakai^{51,133}, M. A. Saleh¹⁴¹, J. Salzwedel¹⁸, S. Sambyal¹⁰³, V. Samsonov^{85,98}, A. Sandoval⁷⁵, D. Sarkar¹³⁹, N. Sarkar¹³⁹, P. Sarma⁴⁴, M. H. P. Sas⁶⁴, E. Scapparone⁵⁴, F. Scarlassara²⁹, R. P. Scharenberg¹⁰⁸, H. S. Scheid⁷¹, C. Schiaua⁸⁹, R. Schicker¹⁰⁶, C. Schmidt¹⁰⁹, H. R. Schmidt¹⁰⁵, M. O. Schmidt¹⁰⁶, M. Schmidt¹⁰⁵, N. V. Schmidt⁷¹, S. Schuchmann¹⁰⁶, J. Schukraft³⁵, Y. Schutz^{35,117,135}, K. Schwarz¹⁰⁹, K. Schweda¹⁰⁹, G. Scioli²⁷, E. Scomparin⁵⁹, R. Scott¹³⁰, M. Šeščík⁴⁰, J. E. Seger⁹⁹, Y. Sekiguchi¹³², D. Sekihata⁴⁷, I. Selyuzhenkov^{85,109}, K. Senosi⁷⁷, S. Senyukov^{3,35,135}, E. Serradilla^{10,75}, P. Sett⁴⁸, A. Sevcenco⁶⁹, A. Shabanov⁶³, A. Shabetai¹¹⁷, R. Shahoyan³⁵, W. Shaikh¹¹², A. Shangaraev¹¹⁵, A. Sharma¹⁰¹, A. Sharma¹⁰³, M. Sharma¹⁰³, M. Sharma¹⁰³, N. Sharma^{101,130}, A. I. Sheikh¹³⁹, K. Shigaki⁴⁷, Q. Shou⁷, K. Shtejer^{9,26}, Y. Sibiriak⁹², S. Siddhanta⁵⁵, K. M. Sielewicz³⁵, T. Siemiarczuk⁸⁸, D. Silvermyr³⁴, C. Silvestre⁸³, G. Simatovic¹⁰⁰, G. Simonetti³⁵, R. Singaraju¹³⁹, R. Singh⁹⁰, V. Singhal¹³⁹, T. Sinha¹¹², B. Sitar³⁸, M. Sitta³², T. B. Skaali²¹, M. Słupecki¹²⁸, N. Smirnov¹⁴³, R. J. M. Snellings⁶⁴, T. W. Snellman¹²⁸, J. Song¹⁹, M. Song¹⁴⁴, F. Soramel²⁹, S. Sorensen¹³⁰, F. Sozzi¹⁰⁹, E. Spiriti⁵¹, I. Sputowska¹²¹, B. K. Srivastava¹⁰⁸, J. Stachel¹⁰⁶, I. Stan⁶⁹, P. Stankus⁹⁷, E. Stenlund³⁴, D. Stocco¹¹⁷, M. M. Storetvedt³⁷, P. Strmen³⁸, A. A. P. Suaide¹²⁴, T. Sugitate⁴⁷, C. Suire⁶², M. Suleymanov¹⁵, M. Suljic²⁵, R. Sultanov⁶⁵, M. Šumbera⁹⁶, S. Sumowidagdo⁵⁰, K. Suzuki¹¹⁶, S. Swain⁶⁸, A. Szabo³⁸, I. Szarka³⁸, U. Tabassam¹⁵, J. Takahashi¹²⁵, G. J. Tambave²², N. Tanaka¹³³, M. Tarhini⁶², M. Tariq¹⁷, M. G. Tarzila⁸⁹, A. Tauro³⁵, G. Tejada Muñoz², A. Telesca³⁵, K. Terasaki¹³², C. Terrevoli²⁹, B. Teyssier¹³⁴, D. Thakur⁴⁹, S. Thakur¹³⁹, D. Thomas¹²², F. Thoresen⁹³, R. Tieulent¹³⁴, A. Tikhonov⁶³, A. R. Timmins¹²⁷, A. Toia⁷¹, S. Tripathy⁴⁹, S. Trogolo²⁶, G. Trombetta³³, L. Tropp⁴⁰, V. Trubnikov³, W. H. Trzaska¹²⁸, B. A. Trzeciak⁶⁴, T. Tsuji¹³², A. Tumkin¹¹¹, R. Turrisi⁵⁷, T. S. Tveter²¹, K. Ullaland²², E. N. Umaka¹²⁷, A. Uras¹³⁴, G. L. Usai²⁴, A. Utrobicic¹⁰⁰, M. Vala^{66,119}, J. Van Der Maarel⁶⁴, J. W. Van Hoorne³⁵, M. van Leeuwen⁶⁴, T. Vanat⁹⁶, P. Vande Vyvre³⁵, D. Varga¹⁴², A. Vargas², M. Vargyas¹²⁸, R. Varma⁴⁸, M. Vasileiou⁸⁷, A. Vasiliev⁹², A. Vauthier⁸³, O. Vázquez Doce^{36,107}, V. Vechernin¹³⁸, A. M. Veen⁶⁴, A. Vulture²², E. Vercellin²⁶, S. Vergara Limón², R. Vernet⁸, R. Vértesi¹⁴², L. Vickovic¹²⁰, S. Vigolo⁶⁴, J. Viinikainen¹²⁸, Z. Vilakazi¹³¹, O. Villalobos Baillie¹¹³, A. Villatoro Tello², A. Vinogradov⁹², L. Vinogradov¹³⁸, T. Virgili³⁰, V. Vislavicius³⁴, A. Vodopyanov⁷⁸, M. A. Völkl^{105,106}, K. Voloshin⁶⁵, S. A. Voloshin¹⁴¹, G. Volpe³³, B. von Haller³⁵, I. Vorobyev^{36,107}, D. Voscek¹¹⁹, D. Vranic^{35,109}, J. Vrláková⁴⁰, B. Wagner²², H. Wang⁶⁴, M. Wang⁷, D. Watanabe¹³³, Y. Watanabe¹³², M. Weber¹¹⁶, S. G. Weber¹⁰⁹, D. F. Weiser¹⁰⁶, S. C. Wenzel³⁵, J. P. Wessels⁷², U. Westerhoff⁷², A. M. Whitehead¹⁰², J. Wiechula⁷¹, J. Wikne²¹, G. Wilk⁸⁸, J. Wilkinson^{106,54}, G. A. Willems⁷², M. C. S. Williams⁵⁴, E. Willsher¹¹³, B. Windelband¹⁰⁶, W. E. Witt¹³⁰, S. Yalcin⁸¹, K. Yamakawa⁴⁷, P. Yang⁷, S. Yano⁴⁷, Z. Yin⁷, H. Yokoyama^{83,133}, I.-K. Yoo^{19,35}, J. H. Yoon⁶¹, V. Yurchenko³, V. Zaccaro^{59,93}, A. Zaman¹⁵, C. Zampolli³⁵, H. J. C. Zanoli¹²⁴, N. Zardoshti¹¹³, A. Zarochentsev¹³⁸, P. Závada⁶⁷, N. Zaviyalov¹¹¹, H. Zbroszczyk¹⁴⁰, M. Zhalov⁹⁸, H. Zhang^{7,22}, X. Zhang⁷, Y. Zhang⁷, C. Zhang⁶⁴, Z. Zhang^{7,82}, C. Zhao²¹, N. Zhigareva⁶⁵, D. Zhou⁷, Y. Zhou⁹³, Z. Zhou²², H. Zhu²², J. Zhu⁷, X. Zhu⁷, A. Zichichi^{12,27}, A. Zimmermann¹⁰⁶, M. B. Zimmermann^{35,72}, G. Zinovjev³, J. Zmeskal¹¹⁶, S. Zou⁷

- ¹ A.I. Alikhanyan National Science Laboratory (Yerevan Physics Institute) Foundation, Yerevan, Armenia
- ² Benemérita Universidad Autónoma de Puebla, Puebla, Mexico
- ³ Bogolyubov Institute for Theoretical Physics, Kiev, Ukraine
- ⁴ Department of Physics and Centre for Astroparticle Physics and Space Science (CAPSS), Bose Institute, Kolkata, India
- ⁵ Budker Institute for Nuclear Physics, Novosibirsk, Russia
- ⁶ California Polytechnic State University, San Luis Obispo, CA, USA
- ⁷ Central China Normal University, Wuhan, China
- ⁸ Centre de Calcul de l'IN2P3, Villeurbanne, Lyon, France
- ⁹ Centro de Aplicaciones Tecnológicas y Desarrollo Nuclear (CEADEN), Havana, Cuba
- ¹⁰ Centro de Investigaciones Energéticas Medioambientales y Tecnológicas (CIEMAT), Madrid, Spain
- ¹¹ Centro de Investigación y de Estudios Avanzados (CINVESTAV), Mexico City and Mérida, Mexico
- ¹² Centro Fermi-Museo Storico della Fisica e Centro Studi e Ricerche "Enrico Fermi", Rome, Italy
- ¹³ Chicago State University, Chicago, IL, USA
- ¹⁴ China Institute of Atomic Energy, Beijing, China
- ¹⁵ COMSATS Institute of Information Technology (CIIT), Islamabad, Pakistan
- ¹⁶ Departamento de Física de Partículas and IGFAE, Universidad de Santiago de Compostela, Santiago de Compostela, Spain
- ¹⁷ Department of Physics, Aligarh Muslim University, Aligarh, India
- ¹⁸ Department of Physics, Ohio State University, Columbus, OH, USA
- ¹⁹ Department of Physics, Pusan National University, Pusan, Republic of Korea
- ²⁰ Department of Physics, Sejong University, Seoul, Republic of Korea
- ²¹ Department of Physics, University of Oslo, Oslo, Norway
- ²² Department of Physics and Technology, University of Bergen, Bergen, Norway
- ²³ Dipartimento di Fisica dell'Università 'La Sapienza' and Sezione INFN, Rome, Italy
- ²⁴ Dipartimento di Fisica dell'Università and Sezione INFN, Cagliari, Italy
- ²⁵ Dipartimento di Fisica dell'Università and Sezione INFN, Trieste, Italy
- ²⁶ Dipartimento di Fisica dell'Università and Sezione INFN, Turin, Italy
- ²⁷ Dipartimento di Fisica e Astronomia dell'Università and Sezione INFN, Bologna, Italy
- ²⁸ Dipartimento di Fisica e Astronomia dell'Università and Sezione INFN, Catania, Italy
- ²⁹ Dipartimento di Fisica e Astronomia dell'Università and Sezione INFN, Padua, Italy
- ³⁰ Dipartimento di Fisica 'E.R. Caianiello' dell'Università and Gruppo Collegato INFN, Salerno, Italy
- ³¹ Dipartimento DISAT del Politecnico and Sezione INFN, Turin, Italy
- ³² Dipartimento di Scienze e Innovazione Tecnologica dell'Università del Piemonte Orientale and INFN Sezione di Torino, Alessandria, Italy
- ³³ Dipartimento Interateneo di Fisica 'M. Merlin' and Sezione INFN, Bari, Italy
- ³⁴ Division of Experimental High Energy Physics, University of Lund, Lund, Sweden
- ³⁵ European Organization for Nuclear Research (CERN), Geneva, Switzerland
- ³⁶ Excellence Cluster Universe, Technische Universität München, Munich, Germany
- ³⁷ Faculty of Engineering, Bergen University College, Bergen, Norway
- ³⁸ Faculty of Mathematics, Physics and Informatics, Comenius University, Bratislava, Slovakia
- ³⁹ Faculty of Nuclear Sciences and Physical Engineering, Czech Technical University in Prague, Prague, Czech Republic
- ⁴⁰ Faculty of Science, P.J. Šafárik University, Kosice, Slovakia
- ⁴¹ Faculty of Technology, Buskerud and Vestfold University College, Tonsberg, Norway
- ⁴² Frankfurt Institute for Advanced Studies, Johann Wolfgang Goethe-Universität Frankfurt, Frankfurt, Germany
- ⁴³ Gangneung-Wonju National University, Gangneung, Republic of Korea
- ⁴⁴ Department of Physics, Gauhati University, Guwahati, India
- ⁴⁵ Helmholtz-Institut für Strahlen- und Kernphysik, Rheinische Friedrich-Wilhelms-Universität Bonn, Bonn, Germany
- ⁴⁶ Helsinki Institute of Physics (HIP), Helsinki, Finland
- ⁴⁷ Hiroshima University, Hiroshima, Japan
- ⁴⁸ Indian Institute of Technology Bombay (IIT), Mumbai, India
- ⁴⁹ Indian Institute of Technology Indore, Indore, India
- ⁵⁰ Indonesian Institute of Sciences, Jakarta, Indonesia
- ⁵¹ INFN, Laboratori Nazionali di Frascati, Frascati, Italy

- 52 INFN, Laboratori Nazionali di Legnaro, Legnaro, Italy
- 53 INFN, Sezione di Bari, Bari, Italy
- 54 INFN, Sezione di Bologna, Bologna, Italy
- 55 INFN, Sezione di Cagliari, Cagliari, Italy
- 56 INFN, Sezione di Catania, Catania, Italy
- 57 INFN, Sezione di Padova, Padua, Italy
- 58 INFN, Sezione di Roma, Rome, Italy
- 59 INFN, Sezione di Torino, Turin, Italy
- 60 INFN, Sezione di Trieste, Trieste, Italy
- 61 Inha University, Incheon, Republic of Korea
- 62 Institut de Physique Nucléaire d'Orsay (IPNO), Université Paris-Sud, CNRS-IN2P3, Orsay, France
- 63 Institute for Nuclear Research, Academy of Sciences, Moscow, Russia
- 64 Institute for Subatomic Physics of Utrecht University, Utrecht, The Netherlands
- 65 Institute for Theoretical and Experimental Physics, Moscow, Russia
- 66 Institute of Experimental Physics, Slovak Academy of Sciences, Kosice, Slovakia
- 67 Institute of Physics, Academy of Sciences of the Czech Republic, Prague, Czech Republic
- 68 Institute of Physics, Bhubaneswar, India
- 69 Institute of Space Science (ISS), Bucharest, Romania
- 70 Institut für Informatik, Johann Wolfgang Goethe-Universität Frankfurt, Frankfurt, Germany
- 71 Institut für Kernphysik, Johann Wolfgang Goethe-Universität Frankfurt, Frankfurt, Germany
- 72 Institut für Kernphysik, Westfälische Wilhelms-Universität Münster, Münster, Germany
- 73 Instituto de Ciencias Nucleares, Universidad Nacional Autónoma de México, Mexico City, Mexico
- 74 Instituto de Física, Universidade Federal do Rio Grande do Sul (UFRGS), Porto Alegre, Brazil
- 75 Instituto de Física, Universidad Nacional Autónoma de México, Mexico City, Mexico
- 76 IRFU, CEA, Université Paris-Saclay, Saclay, France
- 77 iThemba LABS, National Research Foundation, Somerset West, South Africa
- 78 Joint Institute for Nuclear Research (JINR), Dubna, Russia
- 79 Konkuk University, Seoul, Republic of Korea
- 80 Korea Institute of Science and Technology Information, Daejeon, Republic of Korea
- 81 KTO Karatay University, Konya, Turkey
- 82 Laboratoire de Physique Corpusculaire (LPC), Clermont Université, Université Blaise Pascal, CNRS-IN2P3, Clermont-Ferrand, France
- 83 Laboratoire de Physique Subatomique et de Cosmologie, Université Grenoble-Alpes, CNRS-IN2P3, Grenoble, France
- 84 Lawrence Berkeley National Laboratory, Berkeley, CA, USA
- 85 Moscow Engineering Physics Institute, Moscow, Russia
- 86 Nagasaki Institute of Applied Science, Nagasaki, Japan
- 87 Physics Department, National and Kapodistrian University of Athens, Athens, Greece
- 88 National Centre for Nuclear Studies, Warsaw, Poland
- 89 National Institute for Physics and Nuclear Engineering, Bucharest, Romania
- 90 National Institute of Science Education and Research, HBNI, Jatni, India
- 91 National Nuclear Research Center, Baku, Azerbaijan
- 92 National Research Centre Kurchatov Institute, Moscow, Russia
- 93 Niels Bohr Institute, University of Copenhagen, Copenhagen, Denmark
- 94 Nikhef, Nationaal instituut voor subatomaire fysica, Amsterdam, The Netherlands
- 95 Nuclear Physics Group, STFC Daresbury Laboratory, Daresbury, UK
- 96 Nuclear Physics Institute, Academy of Sciences of the Czech Republic, Řež u Prahy, Czech Republic
- 97 Oak Ridge National Laboratory, Oak Ridge, TN, USA
- 98 Petersburg Nuclear Physics Institute, Gatchina, Russia
- 99 Physics Department, Creighton University, Omaha, NE, USA
- 100 Physics department, Faculty of Science, University of Zagreb, Zagreb, Croatia
- 101 Physics Department, Panjab University, Chandigarh, India
- 102 Physics Department, University of Cape Town, Cape Town, South Africa
- 103 Physics Department, University of Jammu, Jammu, India

- 104 Physics Department, University of Rajasthan, Jaipur, India
105 Physikalisches Institut, Eberhard Karls Universität Tübingen, Tübingen, Germany
106 Physikalisches Institut, Ruprecht-Karls-Universität Heidelberg, Heidelberg, Germany
107 Physik Department, Technische Universität München, Munich, Germany
108 Purdue University, West Lafayette, IN, USA
109 Research Division and ExtreMe Matter Institute EMMI, GSI Helmholtzzentrum für Schwerionenforschung GmbH, Darmstadt, Germany
110 Rudjer Bošković Institute, Zagreb, Croatia
111 Russian Federal Nuclear Center (VNIIEF), Sarov, Russia
112 Saha Institute of Nuclear Physics, Kolkata, India
113 School of Physics and Astronomy, University of Birmingham, Birmingham, UK
114 Sección Física, Departamento de Ciencias, Pontificia Universidad Católica del Perú, Lima, Peru
115 SSC IHEP of NRC Kurchatov Institute, Protvino, Russia
116 Stefan Meyer Institut für Subatomare Physik (SMI), Vienna, Austria
117 SUBATECH, IMT Atlantique, Université de Nantes, CNRS-IN2P3, Nantes, France
118 Suranaree University of Technology, Nakhon Ratchasima, Thailand
119 Technical University of Košice, Kosice, Slovakia
120 Technical University of Split FESB, Split, Croatia
121 The Henryk Niewodniczanski Institute of Nuclear Physics, Polish Academy of Sciences, Cracow, Poland
122 Physics Department, The University of Texas at Austin, Austin, TX, USA
123 Universidad Autónoma de Sinaloa, Culiacán, Mexico
124 Universidade de São Paulo (USP), São Paulo, Brazil
125 Universidade Estadual de Campinas (UNICAMP), Campinas, Brazil
126 Universidade Federal do ABC, Santo Andre, Brazil
127 University of Houston, Houston, TX, USA
128 University of Jyväskylä, Jyväskylä, Finland
129 University of Liverpool, Liverpool, UK
130 University of Tennessee, Knoxville, TN, USA
131 University of the Witwatersrand, Johannesburg, South Africa
132 University of Tokyo, Tokyo, Japan
133 University of Tsukuba, Tsukuba, Japan
134 Université de Lyon, Université Lyon 1, CNRS/IN2P3, IPN-Lyon, Villeurbanne, Lyon, France
135 Université de Strasbourg, CNRS, IPHC UMR 7178, 67000 Strasbourg, France
136 Università degli Studi di Pavia, Pavia, Italy
137 Università di Brescia, Brescia, Italy
138 V. Fock Institute for Physics, St. Petersburg State University, St. Petersburg, Russia
139 Variable Energy Cyclotron Centre, Kolkata, India
140 Warsaw University of Technology, Warsaw, Poland
141 Wayne State University, Detroit, MI, USA
142 Wigner Research Centre for Physics, Hungarian Academy of Sciences, Budapest, Hungary
143 Yale University, New Haven, CT, USA
144 Yonsei University, Seoul, Republic of Korea
145 Zentrum für Technologietransfer und Telekommunikation (ZTT), Fachhochschule Worms, Worms, Germany
- ^a Deceased
^b Also at: Dipartimento DET del Politecnico di Torino, Turin, Italy
^c Also at: Georgia State University, Atlanta, GA, USA
^d Also at: M.V. Lomonosov Moscow State University, D.V. Skobeltsyn Institute of Nuclear Physics, Moscow, Russia
^e Also at: Department of Applied Physics, Aligarh Muslim University, Aligarh, India
^f Also at: Institute of Theoretical Physics, University of Wrocław, Wrocław, Poland